Postprint of: Ziolkowski P., Ochrymiuk T., Eremeev V., Fluid–solid interaction on a thin platelet with high-velocity flow: vibration modelling and experiment, CONTINUUM MECHANICS AND THERMODYNAMICS (2022), pp. 1-27

Piotr J. Ziółkowski · Tomasz Ochrymiuk · Victor A. Eremeyev

Fluid–solid interaction on a thin platelet with high-velocity flow: vibration modelling and experiment

Abstract The paper concerns the nonlinear behaviour of a thin platelet that is streamlined in an aerodynamic tunnel. The air velocity in the aerodynamic tunnel was at 858.9 km/h or 0.7 Ma (Ma—Mach number is a dimensionless quantity in fluid dynamics representing the ratio of flow velocity past a boundary to the local speed of sound). This experiment was numerically simulated using FSI (fluid–solid interaction) tools, namely the coupling between the strength and flow code. The strength code uses the finite element method, while the flow code is based on the finite volume method. The coupling between the codes was made by means of an interface that transmitted the relevant data and results between the two codes. The paper discusses the methodology of this coupling. The study also highlights the phenomena occurring during the interaction of flow with the plate with emphasis on their nonlinear character.

Keywords Fluid–solid interaction (FSI) · Computational solid dynamics (CSD) · Computational fluid dynamics (CFD)

1 Introduction

Fluid–solid interaction (FSI) describes coupled motions of solids and fluids for the case in this article solid and gases. FSI is a cornerstone in many engineering applications, see, e.g. [1–3]. From the mathematical point of view, FSI relates to a coupled system of partial differential equations. The characteristic feature of FSI is a nonlinearity. The nonlinearities of FSI relate to the nonlinearity of flow as in the case of Navier–Stokes equations, material nonlinearities in solids, and the peculiar nonlinearity in boundary conditions at moving interfaces. This results in the necessity to develop of an efficient numerical tool. In this paper, we discuss such developed numerical tool and present results of modelling of an elastic plate in the wind tunnel. The applied

P. J. Ziółkowski (✉)· V. A. Eremeyev
Mechanics of Materials and Structures, Gdańsk University of Technology, Gdańsk, Poland
E-mail: pjziolkowski@imp.gda.pl

P. J. Ziółkowski · T. Ochrymiuk
Conversion Energy Department, Intitute of Fluid Flow Machinery, Polish Academy of Sciences, Gdańsk, Poland
E-mail: tomasz.ochrymiuk@imp.gda.pl

V. A. Eremeyev
DICAAR, University of Cagliari, Cagliari, Italy
E-mail: victor.eremeev@pg.edu.pl.

V. A. Eremeyev
National Research Lobachevsky State University of Nizhny Novgorod, Nizhny Novgorod, Russia

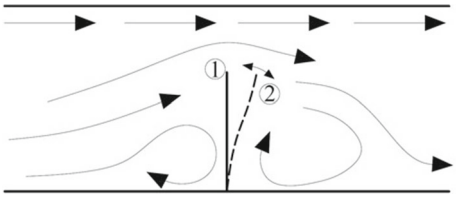

Fig. 1 Nozzle sketch

flow code solves Navier–Stokes equations in the form of averaging turbulent flows by Reynolds method and gives the possibility of a detailed analysis of the structure of flows with vortexes and strong friction layers. The applied non-stationary approach allows the analysis of variable flow field due to aerodynamic phenomena such as vortex separation.

The issue which have been taken into consideration in the paper can be treated as a critical nozzle, in which the mass flow is regulated by a transverse plate mounted in the wall perpendicularly to the flow [in Fig. 1 it is marked as (1)]. A nozzle throat is formed between the plate and the adjacent straight wall, in which a supersonic flow can be created at a sufficiently large pressure difference between the inlet and outlet. In case of a nozzle working as a critical, mass output through the nozzle is proportional to the size of the throat, i.e. to the displacement of the plate. Under the influence of the jet in the nozzle, the plate is inclined, taking the shape, for example, of a dotted line (2) in Fig. 1. In the case of high-velocity flow through a constriction, i.e. flow through a so-called nozzle, there are large pressure variations, which affects the compressibility of the gas in this case, air, which in turn has a significant impact on the formation of velocity and pressure fields. Under flow conditions of the air stream 0.3 Ma (Mach number) and more, the heat produced in the flow and supplied to it must be included in the energy balance. In order to simplify this issue, it is customary to assume adiabatic flow conditions, i.e. no heat exchange between the air in the tunnel and the environment [4,5]. Nowadays critical nozzles are often used in a variety of industrial applications for measurement of the mass flow rates in a wide range of operational conditions [6]. The mass flow rate of working gas is measure by using the flow choking phenomena which occurs at the nozzle throat [7].

1.1 A brief recall of FSI research progress

This paper presents an exemplary numerical methodology for solving FSI problems. The methodology of solving FSI issues has been discussed in many works. For example, Bathe and Hahn [8] have applied procedures to the nonlinear transient analysis of a pipe test using an updated Lagrangian formulation. Luongo and Piccardo [9] have proposed analytical model which deals with the bifurcations mechanisms of coupled flexural galloping in resonant and non-resonant conditions. Piccardo [10] has been studied galloping phenomena in critical conditions on square cylinders, see also [11–14].

Giorgio [15] has proposed a variational model describing a one-dimensional mechanical system in which it is proven that Cattaneo's law for heat conduction can be deduced via a variational argument together with the Lord–Shulman model. The presented formulation can be easily generalized to the three-dimensional cases in FSI modelling. Moreover, when the intrinsic nature of the solid is almost one-dimensional in case under consideration formulation proposed in [16] can be utilized.

Another methodology of solving FSI problems is arbitrary Lagrangian–Eulerian (ALE) approach which combine the advantages of Eulerian and Lagrangian approaches at the same time minimizing the drawbacks. In the ALE approach, a user specifies the combination between the Lagrangian and Eulerian description through the selection of a mesh motion [32]. The Arbitrary Lagrange-Euler method is convenient to use in case of the FSI problems which involve moving boundaries in order to solve Euler equations on a moving domains [17]. Białobrzeski [18] has implemented ALE formulation in model describing the heat and the mass transfer during drying process in spout-fluidized-bed drier taking into account the non-homogenous shrinkage of the material by involving moving boundaries.

The method for solving nonlinear coupled systems resulting from the numerical approximation of FSI problems has been introduced by Fernandez and Moubachir [19] which involves the use of exact cross Jacobians evaluation involving the shape derivative of the fluid state with respect to solid motion perturbations. The three-dimensional case involving regressing solid domains and moving boundaries has been formulated and implemented via the arbitrary Lagrangian–Eulerian finite element method [20], as an example the simulation

of solid-propellant has been used, in which the evolution of fluid–solid interface is governed by combustion law and the transfer of mass and momentum across the interface. A variational arbitrary Lagrangian–Eulerian description has been used to derive general framework for hyperelastostatic and hyperelastodynamic problems by Kuhl and Steinmann [21].

According to the problem and the location of the problem in a given field of physics or technology and depending on the phenomenon that is predominant in the engineering case under consideration (or on the predominant balancing equation), the FSI is divided into [22]: mass-FSI, momentum-FSI and thermal-FSI. Another classification of FSI, this time due to the numerical approach in solving the liquid–solid interaction itself, i.e. the way of implementing momentum exchange between a liquid and a solid in FSI, is divided into partitioned and monolithic. The first is the monolithic approach where fluid and solid domain are a one domain and one solver is responsible for the solution of governing equations [23]. The second approach is the partitioned one [24–26] which is more popular among FSI users because of good stability of solution and being more economical [27]. In the partitioned approach, a large system of the nonlinear equations has to be solved, usually with the use of the iterative solvers for subsystems. The block Newton method [28] is often used to perform these calculations.

Dettmer and Perić [29] have compared exact with inexact strategy in application the block Newton method and suggest that inexact strategy can increase efficiency of partitioned approach for large fluids–solid interaction problems with large elongated interfaces. In the partitioned approach analysis, task is divided into three subtasks: the fluid, the solid, and the mesh. Flow equations are solved by CFD (Computational Fluid Dynamics) solver, and the response of the solid body is obtained by using CSD (Computational Solid Dynamics) solver.

Another classification of the FSI solution procedures is dependent on mesh treatment including: conforming and non-conforming mesh methods. The conforming mesh methods require to adjust meshes to the interface, because interface is treated as physical boundary conditions, where the interface location is part of the solution. In the non-conforming mesh method, interface conditions and location are put as constraints on the model, so the fluid and the solid equations can be solved independently from each other [30].

Authors who have developed the ALE approach in the finite element method format (Donea et al. [31], Belytschko and Kennedy [32], Hughes et al. [33]) have preferred the nomenclature quasi-Eulerian (QE) to emphasize that the structure of the governing equations is very similar to the Eulerian equations. In the present case, large nonlinearities occur both on the fluid side, on the solid side, and in the coupling process between the solids and the liquids. These nonlinearities are already widely described in the literature [3,34,35] and belong to one of the two types: geometrical or physical. It is worth recalling that geometrical nonlinearity results from phenomenon of nonlinear elements occurring in the mathematical description. A very good example of occurring significant geometrical nonlinearities is a situation when the vehicle impacts the cable barrier system [36] or motion of cables [37–42].

Physical nonlinearity, also known as material one, is caused by lack of linear dependence between stress and the strain of the material. Numerical ways to deal with these nonlinearities can be found in the aforementioned literature. Moreover, the description of nonlinearities in the description of Lagrange and Euler differs in certain ways.

1.2 The aim of investigation

The platelet in the wind tunnel was deformed so much that this behaviour cannot be modeled purely linearly. On the solid side, in this case there are only geometrical nonlinearities, but linear behaviour of the material is assumed. One-sided momentum transfer from the fluid to the solid is used in this paper.

The aim of this paper is to investigate the fluctuation of the flow field and the associated changes in plate loading, which in turn leads to oscillations. Oscillation of the platelet in the critical nozzle is important because it leads to changes in the size of the nozzle throat and thus to fluctuations in the mass output of the nozzle, which is undesirable and limits the applicability of the nozzle.

2 Governing equations

2.1 The air motion

In the continuum mechanics, there are known various approaches to the kinematical description [34]. Usually in the fluid mechanics, they use Eulerian description, whereas within the mechanics of solids the Lagrangian

approach seems to be natural. Let us note that there are also other possibilities for the kinematical description of continua. In what follows, the Eulerian description is used as in [43]. The set of the balance equations can be expressed in the following form:

$$\frac{\partial}{\partial t}\begin{Bmatrix}\rho\\ \rho\mathbf{v}\\ \rho e\end{Bmatrix}+\operatorname{div}\begin{Bmatrix}\rho\,\mathbf{v}\\ \rho\,\mathbf{v}\otimes\mathbf{v}\\ \rho\,e\mathbf{v}\end{Bmatrix}=\operatorname{div}\begin{Bmatrix}0\\ \mathbf{t}\\ \mathbf{tv}+\mathbf{q}\end{Bmatrix}+\begin{Bmatrix}0\\ \rho\,\mathbf{t}\\ \rho\,\mathbf{bv}\end{Bmatrix} \tag{1}$$

where ρ is the mass density, $\mathbf{v}$ the continuum particle velocity, $e = c_v T + \frac{1}{2}\mathbf{v}^2$ the total energy, c_v is the specific heat at constant volume, T the temperature, $\mathbf{t}$ the Cauchy stress flux, $q = -\lambda\nabla T$ the molecular heat flux defined by Fourier law (λ is thermal conductivity coefficient), $\mathbf{b}$ the earth acceleration, $\rho\,\mathbf{v}\otimes\mathbf{v}$ means a convective flux of momentum. This component indicates that the momentum of the fluid particle is convectionally transported with velocity $\mathbf{v}$. Regardless of the fluid, this component causes geometrical nonlinearity. The Cauchy stress flux can be divided into an elastic part and a diffusive part:

$$\mathbf{t} = \mathbf{P} + \tau^c \tag{2}$$

where $\mathbf{P}$ is an elastic momentum flux which is reversible and τ^c is a total diffusive momentum flux which describes irreversible phenomena such as viscosity. The elastic part $\mathbf{P}$ is the spherical pressure tensor in the case of liquids which cannot transfer an elastic shear stress. In the case of solids, $\mathbf{P}$ is in the full form of the elastic stress tensor [44,45]:

$$\mathbf{P} = -p\mathbf{I} = -p\delta_{ij}\mathbf{e}_i\otimes\mathbf{e}_j \quad \text{for fluid} \tag{3}$$

$$\mathbf{P} = \sigma = \sigma_{ij}\mathbf{e}_i\otimes\mathbf{e}_j \quad \text{for solid} \tag{4}$$

where p represents a thermodynamical pressure, δ_{ij} is the Kronecker symbol, $\mathbf{e}_i$ base vectors, $\otimes$ is the dyadic product, and σ is the Piola–Kirchhoff second tensor [34,46].

The total diffusive momentum flux is defined in the following form:

$$\tau^c = \tau + \mathbf{R} + \mathbf{D} + \cdots \tag{5}$$

where τ is a viscous momentum flux, $\mathbf{R}$ is a turbulent momentum flux, $\mathbf{D}$ is a diffusion momentum flux, "*ldots*" represents other fluxes that have been neglected in these considerations, e.g. transpirational momentum flux [47,48]. The viscous momentum flux is expressed by the following equation:

$$\tau = -\frac{2}{3}\mu I_d\mathbf{I} + 2\mu\mathbf{d} \tag{6}$$

where μ is the molecular viscosity, $\mathbf{d} = \frac{1}{2}(\mathbf{v}\otimes\nabla + \nabla\otimes\mathbf{v})$ is the strain rate tensor, and $I_d = \operatorname{tr}\mathbf{d}$ is the first invariant of the strain rate.

The turbulent momentum flux $\mathbf{R}$ also known as turbulent Reynolds stress can be written as an analogy to the Newtonian fluid model:

$$\mathbf{R} = -\frac{2}{3}\mu_t I_d\mathbf{I} + 2\mu_t\mathbf{d} \tag{7}$$

where μ_t is the turbulent viscosity coefficient. In what follows we consider in Eq. (5) τ and $\mathbf{R}$ only. For solids, no evolution equations are used, while on the fluid side, the Spalart–Allmaras turbulence evolution model is used [49].

It was assumed that the fluid domain is modelled as compressible Newtonian fluid.

2.2 The platelet motion

In order to describe geometric nonlinearities in the motion of the considered steel platelet let consider the material domain denoted as $R_{\mathbf{X}} \subset \mathbf{R}^{n_{\mathrm{sd}}}$, with n_{sd} spatial dimensions, with the material particles $\mathbf{X}$ and the spatial domain $R_{\mathbf{x}}$, consisting of spatial points $\mathbf{x}$. Now the observation of the steel platelet is continued in the motion. The motion of material points of the platelet relates the material coordinates, $\mathbf{X}$, to the spatial ones, $\mathbf{x}$ through the introduction of the motion vector $\mathbf{u}$:

$$\mathbf{u} = \mathbf{x} - \mathbf{X} \tag{8}$$

and the tensor of the deformation gradient which here is adopted as basic measure of the platelet deformation during its motion:

$$\mathbf{F} = \mathrm{Grad}\mathbf{x} = \mathbf{x} \otimes \nabla_{\mathbf{X}} = \left(\frac{\partial}{\partial X_A}\mathbf{x}\right) \otimes \mathbf{E}_A = x_{i,A}\mathbf{e}_i \otimes \mathbf{E}_A = \mathrm{Grad}(\mathbf{X} + \mathbf{u}) = \mathbf{I} + \mathrm{Grad}\mathbf{u} \tag{9}$$

the representation of this measure of deformation is a 3×3 $x_{i,A}$ matrix, whose determinant is indicated by the letter $\mathcal{J}$:

$$\mathcal{J} = \mathrm{det}\mathbf{F} = \mathrm{det} \mid x_{i,A} \mid \tag{10}$$

using the deformation gradient and several other identities, it expresses the balance of mass in Lagrange's form as below:

$$\rho = \rho_0 \mathcal{J}^{-1} \tag{11}$$

where ρ is actual density of deformed platelet and ρ_0 is initial density of the undeformed platelet.

Momentum balance can be expressed in the following form:

$$\rho_0 \ddot{\mathbf{x}} = \mathrm{Div}(\mathbf{FS}) + \rho_0 \mathbf{b} \tag{12}$$

where $\ddot{\mathbf{x}}$ is acceleration of material particles of the platelet, $\mathbf{S}$ is the momentum flux and $\mathbf{b} = -9.81\mathbf{e}_z$ is the vector of the gravitional acceleration (negligible in that case). Energy balance can be written as follows:

$$\rho_0 \dot{u} = \mathbf{S} \cdot \dot{\mathbf{E}} + \mathrm{Div}\mathbf{Q} + \rho_0 \mathbf{r} \tag{13}$$

where u means internal energy, r is the radiation source (negligible in that case), and $\mathbf{E}$ is the Green strain tensor expressed by the following formula:

$$\mathbf{E} = \frac{1}{2}(\mathbf{F}^T\mathbf{F} - \mathbf{I}) = E_{AB}\mathbf{E}_A \otimes \mathbf{E}_B = \frac{1}{2}(u_{A,B} + u_{B,A} + u_{A,C}u_{C,B})\mathbf{E}_A \otimes \mathbf{E}_B = \mathbf{E}^T \tag{14}$$

In the above approach, there appeared divergence (Div) calculated in the determination to the non-deformed configuration, which also determined the appropriate fluxes of momentum and heat.

$$\mathbf{S} = \mathcal{J}\mathbf{F}^{-1}\mathbf{T}\mathbf{F}^{-T} = \mathbf{S}^T = S_{AB}\mathbf{E}_A \otimes \mathbf{E}_B \tag{15}$$

$$\mathbf{Q} = \mathcal{J}\mathbf{F}^{-1}\mathbf{q} = Q_A\mathbf{E}_A \tag{16}$$

The momentum and energy fluxes so defined are called Piola–Kirchhoff second stress tensor and Kirchhoff's heat flux, respectively, although in this case no heat exchange between the platelet and the flow or environment is assumed, so the heat flux is equal to zero, $\mathbf{T}$ is Cauchy stress tensor, and $\mathbf{q}$ is total heat flux.

2.3 Momentum FSI boundary conditions

In boundary conditions, specific for momentum-FSI, equality of flux of momentum should be considered as a primary condition which takes place on a fluid–solid, contact surface S. This surface is oriented by versors $\mathbf{n}_f$ and $\mathbf{n}_s$, respectively ($\mathbf{n}_s = -\mathbf{n}_f$). If we denote by $\mathbf{t}_s$ and $\mathbf{t}_f$ the solid and the fluid stress tensors, according to the Cauchy theorem, on the fluid–solid boundary it is obtained:

$$\mathbf{t}_f\mathbf{n}_f + \mathbf{t}_s\mathbf{n}_s = 0 \tag{17}$$

It is a classical equality of boundary forces that can be split on equality of normal components (such as pressure) and equality of tangent component (as friction or mobility forces) [50–52].

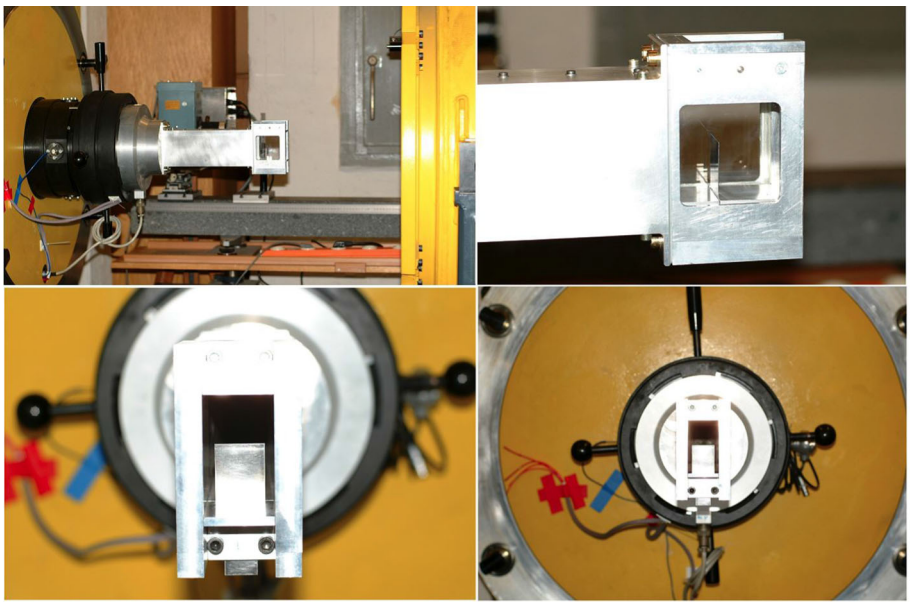

Fig. 2 Rectangular nozzle with mounted the thin platelet

3 Experiment of the flow over thin platelet

The experimental setup was presented in [53]. The thin rectangular platelet is seated between two fixed, rigidly screwed plates, and it is shown in Fig. 2. The way the platelet is fixed divides it into two parts. The first part with dimensions 30 × 24 mm is in the middle of the nozzle, and it is subjected to the flow. The second part, which is rigidly fixed in the nozzle with a protruding tip. The width of the wider part of the platelet is 30 mm, and the narrower part is 20 mm. The total height of the platelet is 80 mm, but the wider part of the platelet is 50 mm in height and the narrower part is 30 mm. The dimensions of platelet are presented in Fig. 3. The platelet is made of a 0.2-mm-thick structural steel. Its and material properties are assumed as follows: density $\rho = 7860\,[\mathrm{kg/m^3}]$, Young modulus $E = 210\,[\mathrm{GPa}]$, Poisson ratio $\nu = 0.3$ [–], coefficient of thermal expansion $\alpha_\theta = 1.2\mathrm{e}{-}05$ [1/K]. The experiment was carried out in the DRL aerodynamical tunnel in Göttingen, which has a wide spectrum of Mach and Reynolds numbers. The tunnel is also equipped with a rectangular nozzle, which was used in the experiment.

Flow characteristics have been measured by a quantitative schlieren method, and the vibration frequency of the plate has been measured using a photodiode connected to an oscilloscope. The natural frequencies and forced by flow frequencies in the range 0.3–0.9 Ma were measured. In the experiment, the flow with the appropriate Mach number is obtained by lowering the pressure in the tank behind the nozzle outlet to the appropriate value in the absence of the platelet in the duct. The air was taken from the environment. The voltage obtained from the oscilloscope for free vibrations and vibrations due to 0.7 Ma air flow is shown in Fig. 4. Plots of the fast Fourier transform for these vibrations are presented in Fig. 5. From Fig. 5, it can be deduced that the frequency of forced vibrations is about 300 Hz and of free vibrations about 260 Hz. In both cases, a small peak of about 150 Hz is visible.

Figure 6 shows the platelet deflection caused by air flow 0.7 Ma, which is approximately 6.1 mm.

4 FSI analysis of the flow over thin platelet

Finite element method [54] was used to determine the deformations and vibrations of the structure. For the calculations presented in the paper, 20 nodal isoparametric elements were used [54] with reduced integration. The equations of motion of the vibrating platelet were integrated using Newmark's direct integration method [55]. In the paper has been used the code for transferring the results between the flow and the mechanical part, which is a basic integration role. Both the time step and the calculation grid are different in the flow and mechanical parts. The integration of codes therefore requires an efficient and accurate transition between them. The flow code provides a temporary distribution of pressure on the tested surfaces, and the mechanical

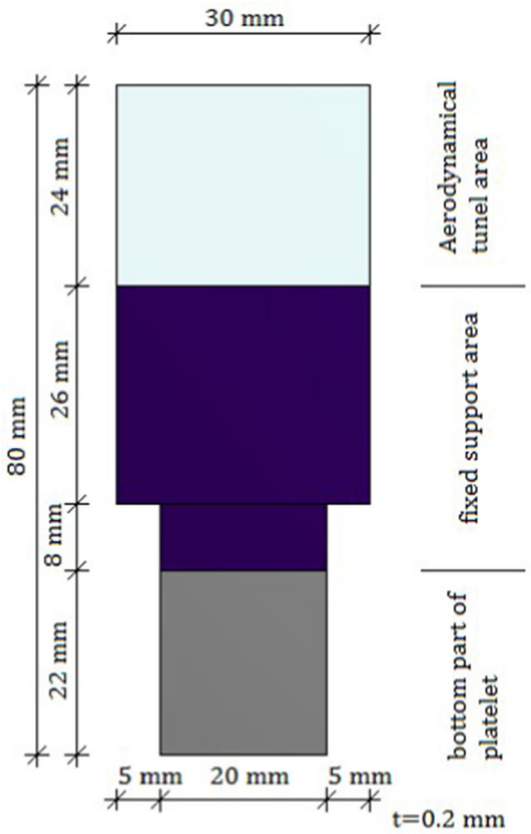

Fig. 3 Dimensions of the platelet with a description of the placement

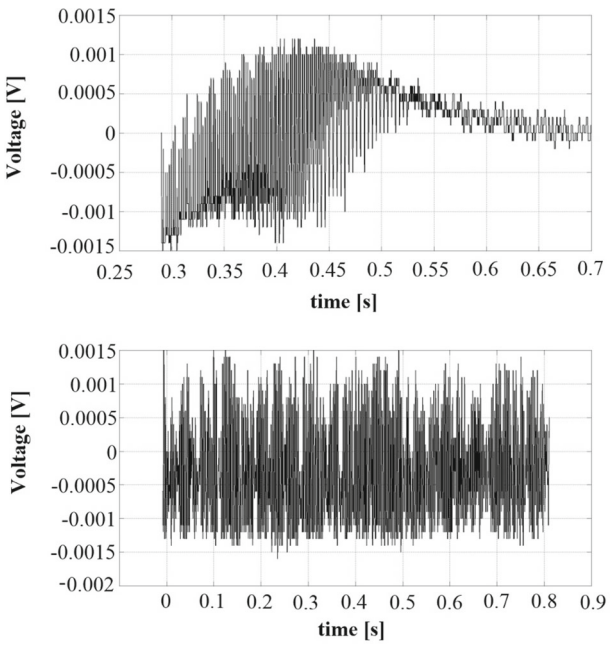

Fig. 4 Measured voltage for natural frequencies (top) and frequencies forced by 0.7 Ma flow (bottom)

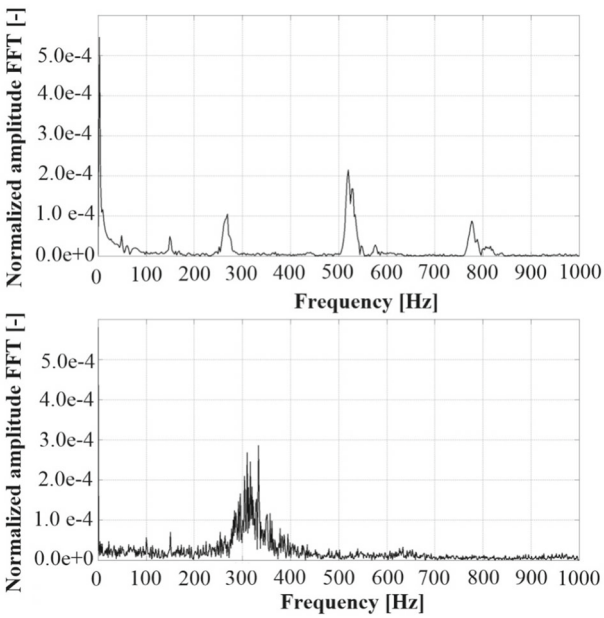

Fig. 5 Fast Fourier Transform for natural frequencies (top) and and frequencies forced by 0.7 Ma flow (bottom)

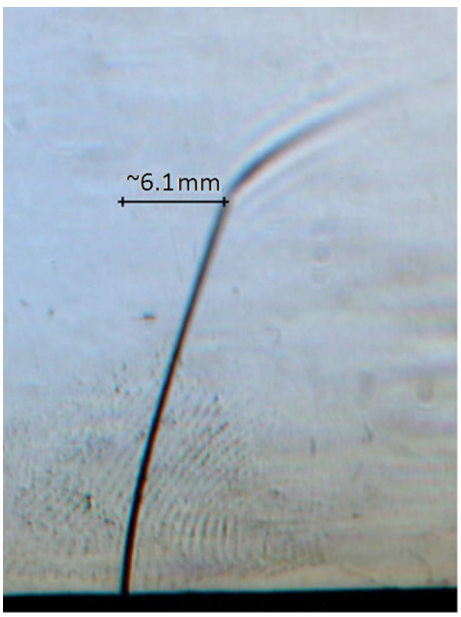

Fig. 6 Deflection of the 0.2-mm-thick platelet at 0.7 Ma flow

code gives the deformations on the basis of which a new grid is built in the flow code. The described package can be used for various aeroelasticity issues such as wing oscillation due to aerodynamic forces, vibrations of turbine and compressor blades or vibrations of slender structures under wind pressure.

Geometric points were read from a photograph taken during the experiment. The resulting geometry is only a good approximation of the actual geometry. This is due to out-of-sharp photos and inaccuracies in the method of reading points from them. The open space, which actually ended up in the experiment, was transformed in the computational model into a significantly elongated channel, whose geometry with marked boundary conditions is visible in Fig. 7. The upper part of Fig. 7 shows boundary conditions for flow calibration, and the lower part of Fig. 7 shows boundary conditions for flow with the platelet. The introduced modification of the geometry simplified the computational model, reduced the number of finite volumes and allowed for the

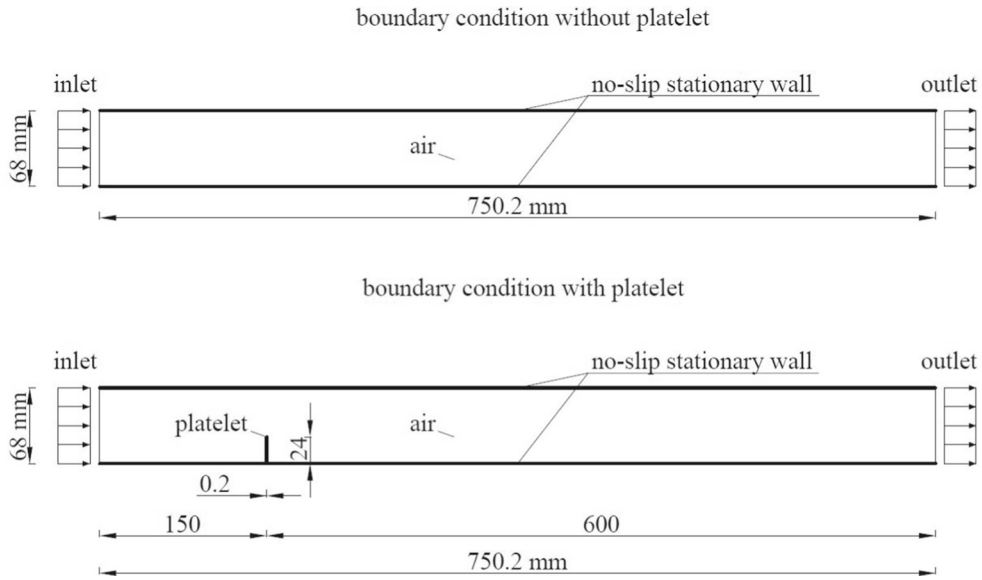

Fig. 7 Boundary conditions without the platelet (top) and with the platelet (bottom)

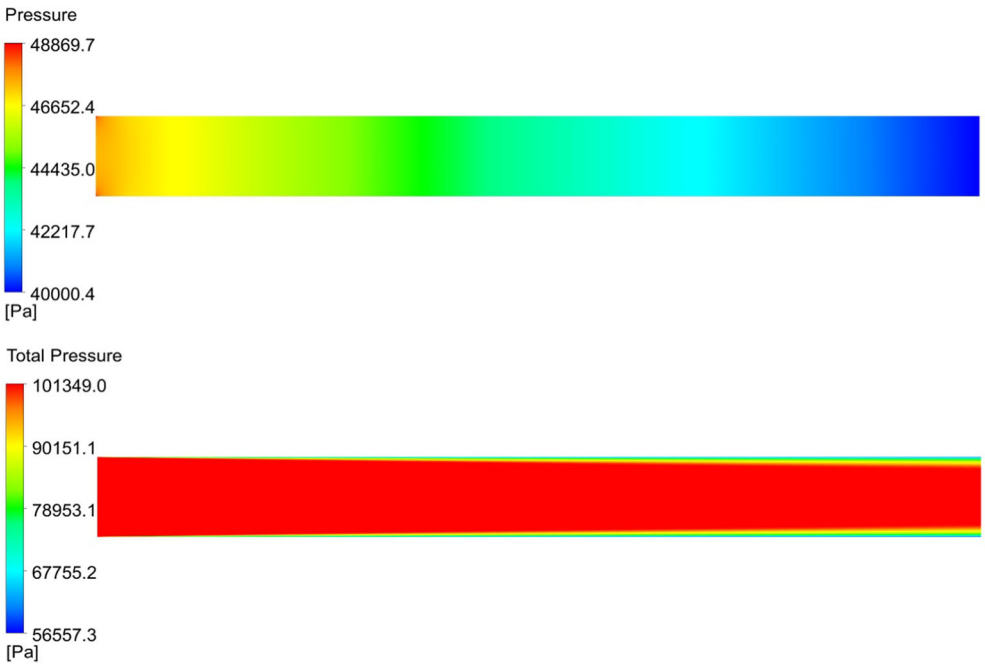

Fig. 8 Static pressure distribution along the entire computational geometry (top) and total pressure distribution along the entire computational geometry (bottom)

correct assignment of boundary conditions. Numerical solution of the air flow over the platelet is based on the finite volume method [43]. Pressure-based coupled solver has been utilized which pressure and momentum solves simultaneously [43]. The air domain is divided into a set of control volumes, and using this set the conservation equations for mass, momentum and energy are solved. The FSI calculation was performed on a quasi-two-dimensional model. This means that a three-dimensional model with a mesh thickness of one finite element (one finite volume) with the condition of planar symmetry on both sides of the model was used.

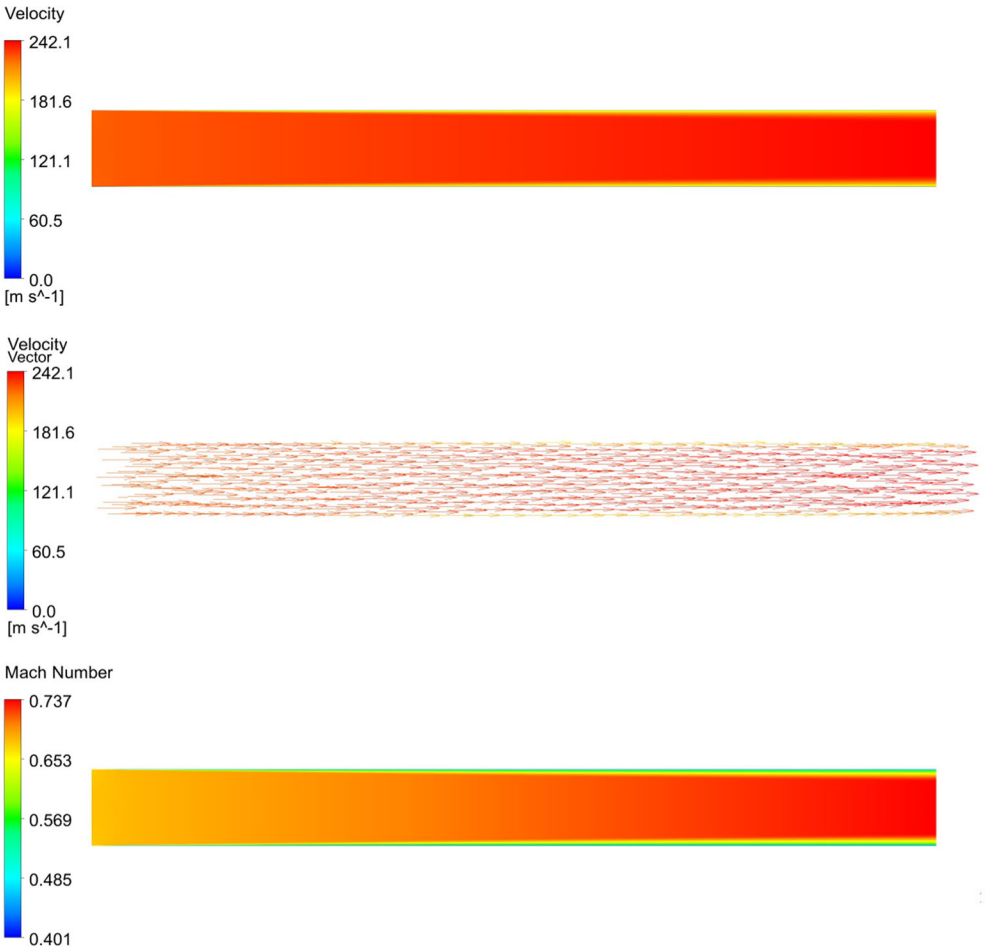

Fig. 9 Velocity distribution along the entire computational geometry (top), velocity vectors along the entire computational geometry (middle) and Mach number distribution along the entire computational geometry (bottom)

4.1 The calibration of the boundary conditions in CFD

The first step in the numerical task was to select appropriate boundary conditions for the channel that would correspond to the flow velocity of 0.7 Ma, for this purpose a simulation of the flow under stationary conditions for the channel without the presence of a plate was performed. The following air parameters were assumed: for density the model of ideal gas was adopted, specific heat was assumed as constant with value 1006.43 [J/kg K], coefficient of thermal conductivity with value 0.0242 [W/m K], at viscosity due to high velocity values in flow the Sutherland law [56] with three coefficients (Reference Viscosity $\mu_0 = 1.716\text{e}{-}05$, Reference Temperature $T_0 = 273.11\,\text{K}$ and Effective temperature $S = 110.56\,\text{K}$) was applied. As a model of turbulence evolution, a one-equation Spalart–Allmaras model [49] was used. The upper part of Fig. 7 illustrates the scheme of the boundary conditions assumed in the calibration of the flow. For the upper and the bottom walls are used the no-slip conditions. The following conditions were set at the inlet: Total pressure = 101,325 [Pa], temperature = 298.15 [K] and at the outlet: Static pressure = 40,000 [Pa] and temperature = 298.15 [K]. The results of the calibration are presented in Figs. 8 and 9. Static and total pressure distributions are shown in Fig. 8, while velocity distribution and vectors along entire computational geometry with Mach number distribution are shown in Fig. 9. Due to adopted boundary condition, mean value of Mach number from entire computational domain is approximately 0.7 Ma and these boundary conditions for the flow domain were adapted for further simulations. Due to the nonlinear character of the equations describing the flow, the selection of appropriate boundary conditions, which later determine the correctness of the whole solution, has an extremely important role.

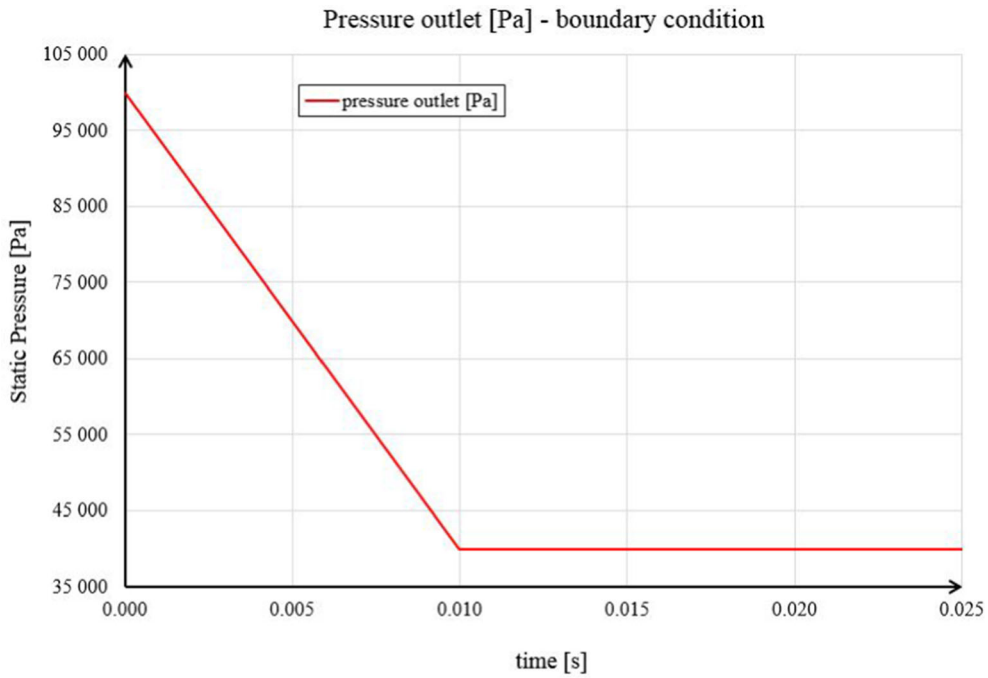

Fig. 10 Static pressure changes at the outlet boundary condition

4.2 FSI analysis: one-sided transfer fluid flow to solid

In this paragraph is shown one-way FSI non-stationary analysis of the thin platelet. The boundary conditions are adopted from previous paragraph; however, in order to obtain results closer to the reality at the outlet, the static pressure varied from 100,000 to 40,000 Pa as shown in Fig. 10. The changing pressure at the outlet is intended to bring the conditions inside the tunnel closer to those prevailing during start-up.

In Figs. 11 and 12 is presented an evolution of the Mach number distribution along the computational domain. The results are shown at specific time steps, namely in Fig. 11 looking from above: 0.00002 s, 0.0025 s, 0.005 s, 0.0075 s, and in Fig. 12 at time steps: 0.01 s, 0.015 s, 0.02 s, 0.025 s. The results of the air density (in Figs. 20 and 21), static pressure (in Figs. 22 and 23), total pressure (in Figs. 24 and 25) and velocity (in Figs. 26 and 27) are presented in a similar way in Appendix at the end of the article. The flow evolution figures clearly show that the flow in the case under consideration has stabilized after approximately 0.015 s. Once the flow has stabilized, the flow evolution figures in the plate extension clearly demonstrate an elongated line that represents a trace of the friction layer. This line is the boundary between the stream flowing from the plate and the separation created behind the plate. The friction layer is associated with a change in density, the evolution of which in the air flow is shown in Figs. 20 and 21. The importance of compressibility is due to the high speeds in the nozzle. As illustrated in Figs. 11 and 12, the Mach number exceeds 1, so the nozzle operates under critical conditions. In the nozzle, you can see a wandering air wave and its diffraction; this is related to the change in the nozzle cross-section caused by the presence of the platelet.

The following section will show the numerical response of the platelet to the non-stationary load of the pressure of the flowing air stream in the tunnel. The pressure transfer was carried out through a special interface. The main task of the interface connecting flow and strength calculations is the proper transfer of data and results between the individual codes. In the case under consideration, it was necessary to determine the displacement of the plate on the basis of the pressure values acting on the surface of the plate. The coupling of the calculation codes was achieved by one-way pressure transfer from flow to plate. The pressure transfer from the flow code to the structural code was done with a time step of 2e−05 s. The operation of the strength program is based on the finite element method (FEA). The plate is modeled with 20 node elements. As an input data into finite element method code, the values of the forces obtained from the pressure field acting on the plate are entered. The oscillations shown in Fig. 13 represent the plate's response to airflow in the tunnel. The inclination of the platelet increases as the difference in pressure at the inlet and outlet increases. The inclination is stabilized after approx. 0.015 s, which corresponds to the moment of flow stabilization. The set inlet pressure became

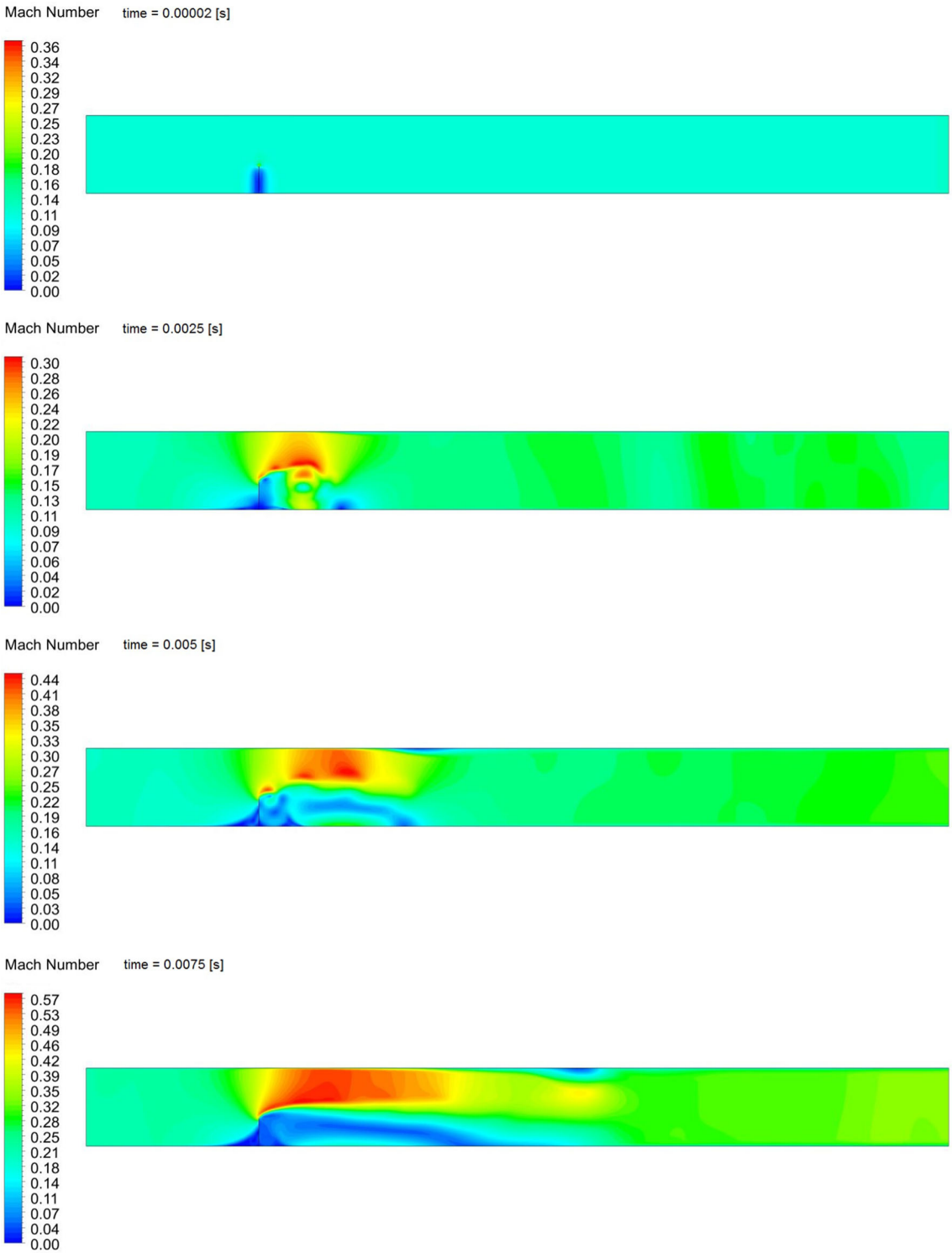

Fig. 11 Mach number distribution along the entire computational geometry at the time points = 0.00002, 0.0025, 0.005, 0.0075

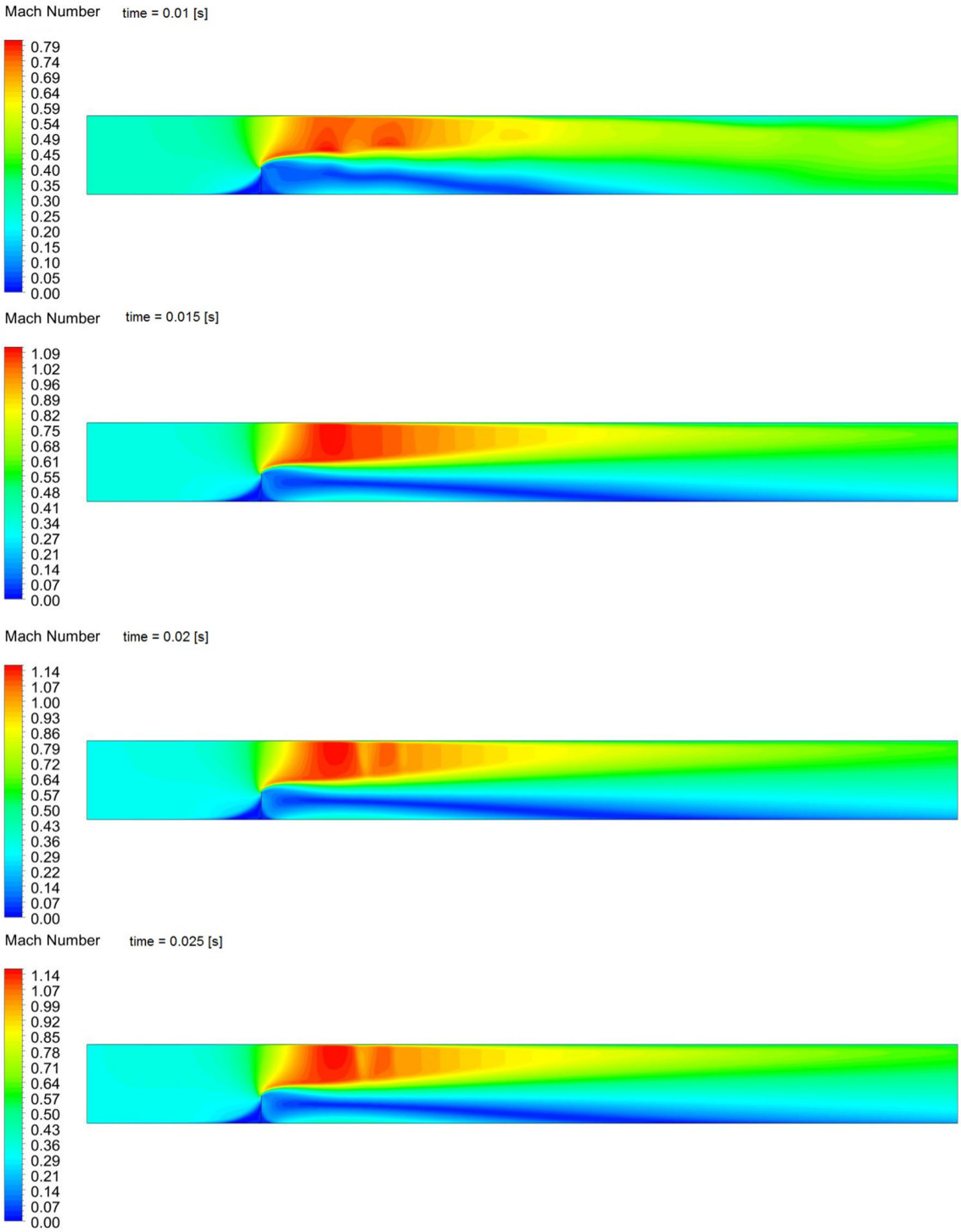

Fig. 12 Mach number distribution along the entire computational geometry at the time points = 0.01, 0.015, 0.02, 0.025

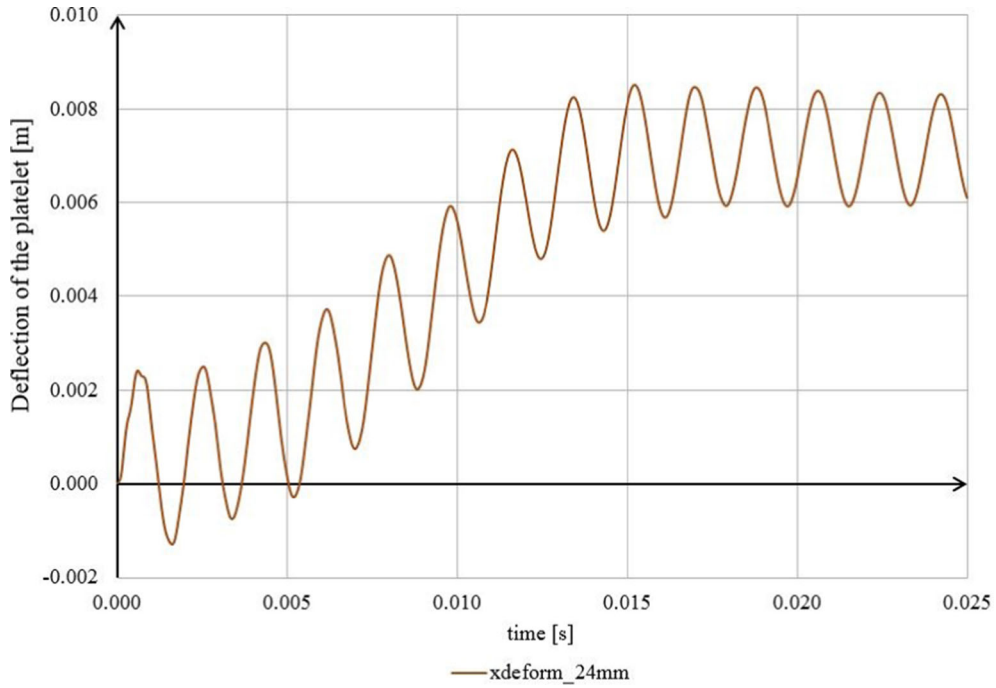

Fig. 13 Maximum deflection of the platelet in *x* direction under non-stationary pressure load

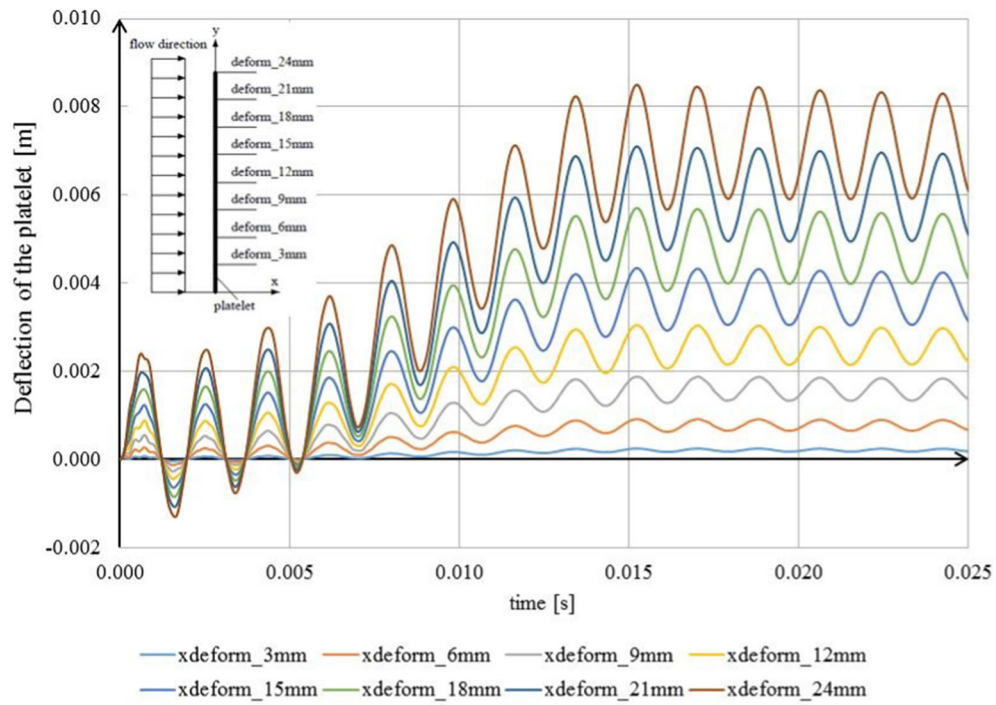

Fig. 14 Deflection of the platelet in *x* direction under non-stationary pressure load

constant after a time of 0.01 s in the simulation. It took 0.005 s of time for the flow to stabilize at the already constant inlet pressure. The frequency of oscillation of platelet induced by the flow reaches approximately 555 Hz. The initial value of the oscillation is about 3 mm in simulation, although over time this value decreases to about 2 mm. The average inclination of the platelet after flow stabilization in the simulation was read as 7.1 mm. This value is 16% higher than the platelet's inclination value in Fig. 6.

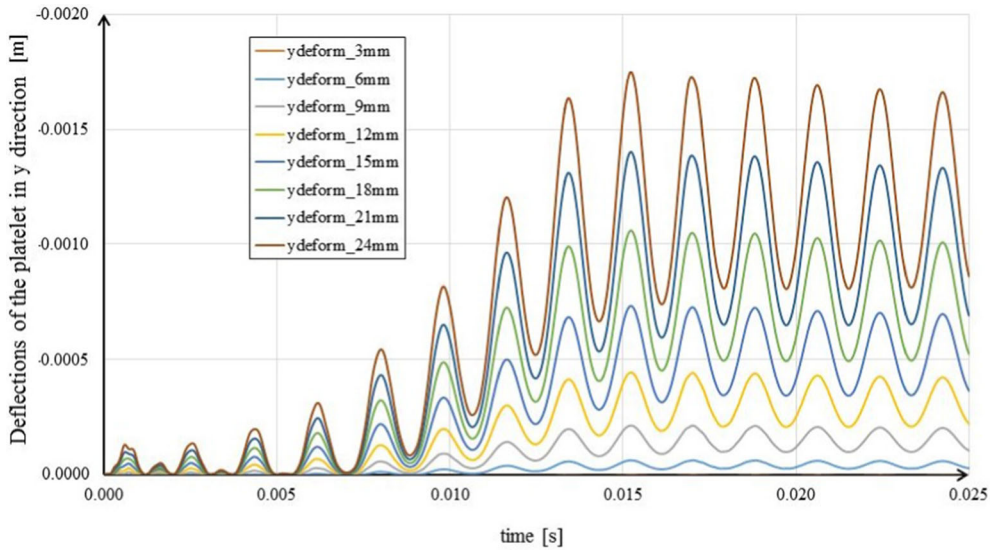

Fig. 15 Deflection of the platelet in *y* direction under non-stationary pressure load

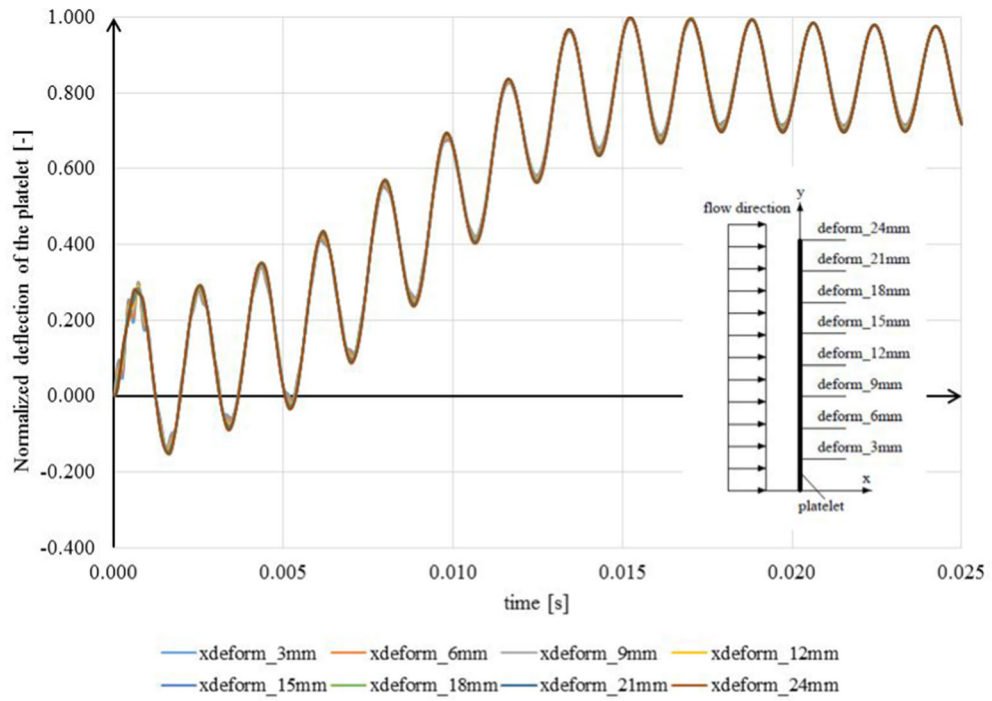

Fig. 16 Normalized deflection of the platelet in *x* direction under non-stationary pressure load

Figure 14 shows the behaviour of the simulated plate for 8 control points at different plate heights (3 mm, 6 mm, 9 mm, 12 mm, 15 mm, 18 mm, 21 mm, 24 mm) in *x* direction (horizontal), while Fig. 15 shows this for *y* direction (vertical).

Figures 16, 17 and 18 show a standardized deflection of the platelet in the *x* direction (horizontal) at 8 points on the platelet evenly spaced out. Standardization has been carried out in relation to the highest value of the deflection *x* for individual points. The aim of standardization was to show the qualitative behaviour of the platelet in the flow.

From Fig. 17, it can be concluded that the initial moment of the simulation, which in the flow part of the simulation corresponded to an increase in the pressure difference at the inlet and outlet of the flow channel, is accompanied by a strongly non-stationary platelet response. The behaviour of the plate along with the

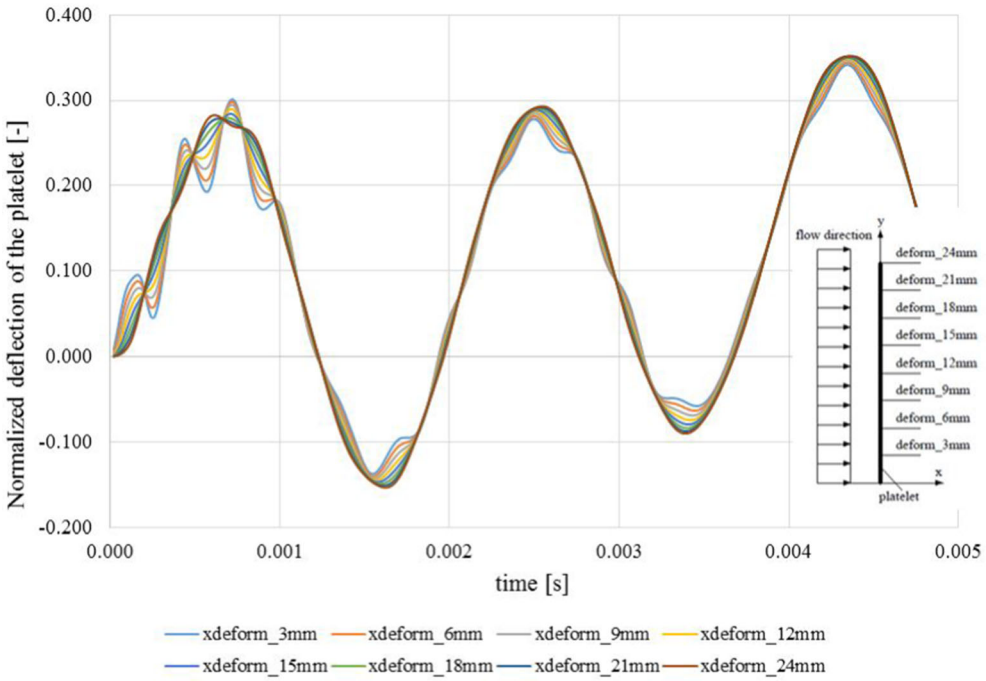

Fig. 17 Normalized deflection of the platelet in x direction under non-stationary pressure load at time 0–0.005 s

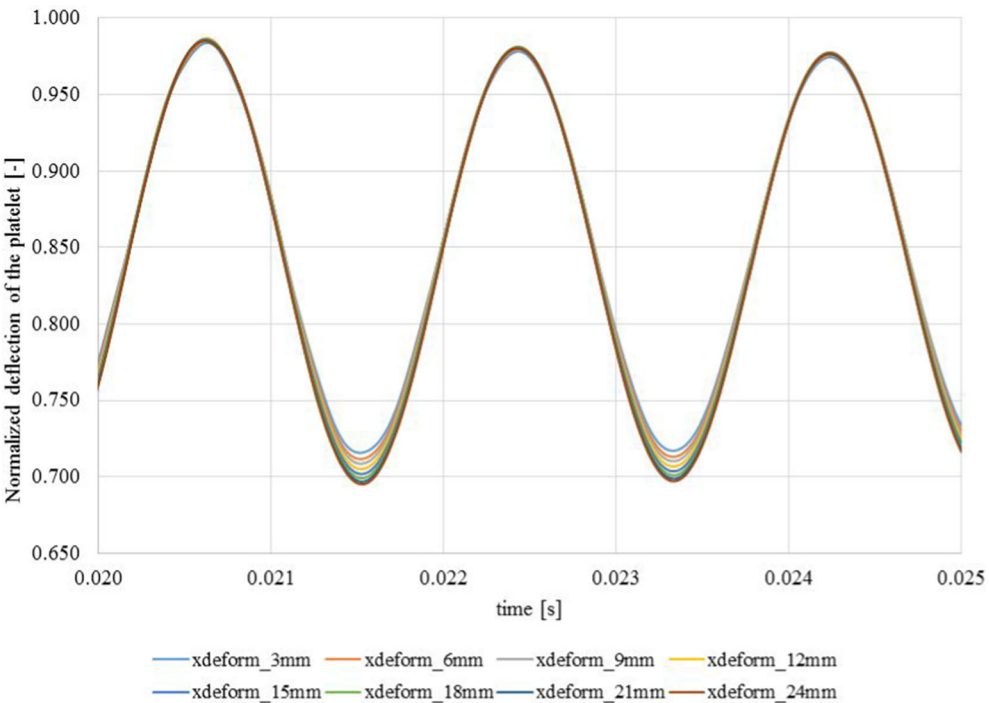

Fig. 18 Normalized deflection of the platelet in x direction under non-stationary pressure load at time 0.02–0.025 s

stabilization of the flow also stabilizes, as can be seen in Fig. 18. Figure 18 shows that in a stabilized flow in the model under consideration, the way the platelet is mounted in the channel influences the nonlinearity of oscillations.

In Fig. 19 is shown comparison of the numerical solution to experiment at time 0.015–0.0225 s of the simulation. The platelet deflection values for the experimental and numerical simulation results are comparable,

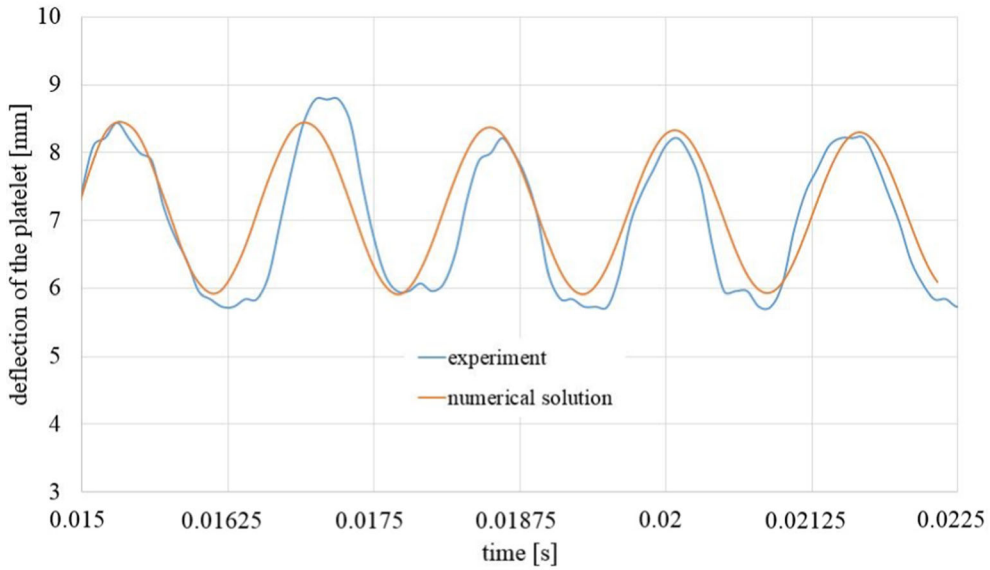

Fig. 19 Comparison of numerical solution to experiment at time 0.015–0.0225 s

although the frequency of vibration differs. The experimental part of the Fig. 19 indicates the high instability of the vibrations and the variability in time. The approach used in the simulation only approximates the vibrations that the plate undergoes in the flow.

5 Conclusions

In this paper, a one-way transfer of momentum from the fluid to the solid has been utilized, as an example, and the oscillations of the platelet are analysed. Overestimated platelet vibration frequency is due to the fact that, in the case considered above, pressures were determined with the flow geometry remaining unchanged and are set as a load on the plate which changed its geometry with each time step; this approach seems to be optimal for small structure displacements, although for large displacements, the use of this method results in overestimation of the structure in design. This method can also be used when the static deformation of the structure is known and the already deformed geometry is applied to the flow model in order to obtain loads from non-stationary air fluctuations. The acceptance of quasi-2D geometry for the calculation also influences the results. In Fig. 2, on both sides of the plate, the space between the tunnel walls and the side surfaces of the plate is visible. The influence of this space on the plate is not yet known to the authors.

Declarations

Conflict of interest The authors declare that they have no conflict of interest.

Appendix: Additional results of flow modelling

The results of CFD calculations are summarized below. The results of density are shown at specific time steps, namely in Fig. 20 looking from above: 0.00002 s, 0.0025 s, 0.005 s, 0.0075 s, and in Fig. 21 at time steps: 0.01 s, 0.015 s, 0.02 s, 0.025 s. The results of the static pressure (in Figs. 22 and 23), total pressure (in Figs. 24 and 25) and velocity (in Figs. 26 and 27) are presented in a similar way.

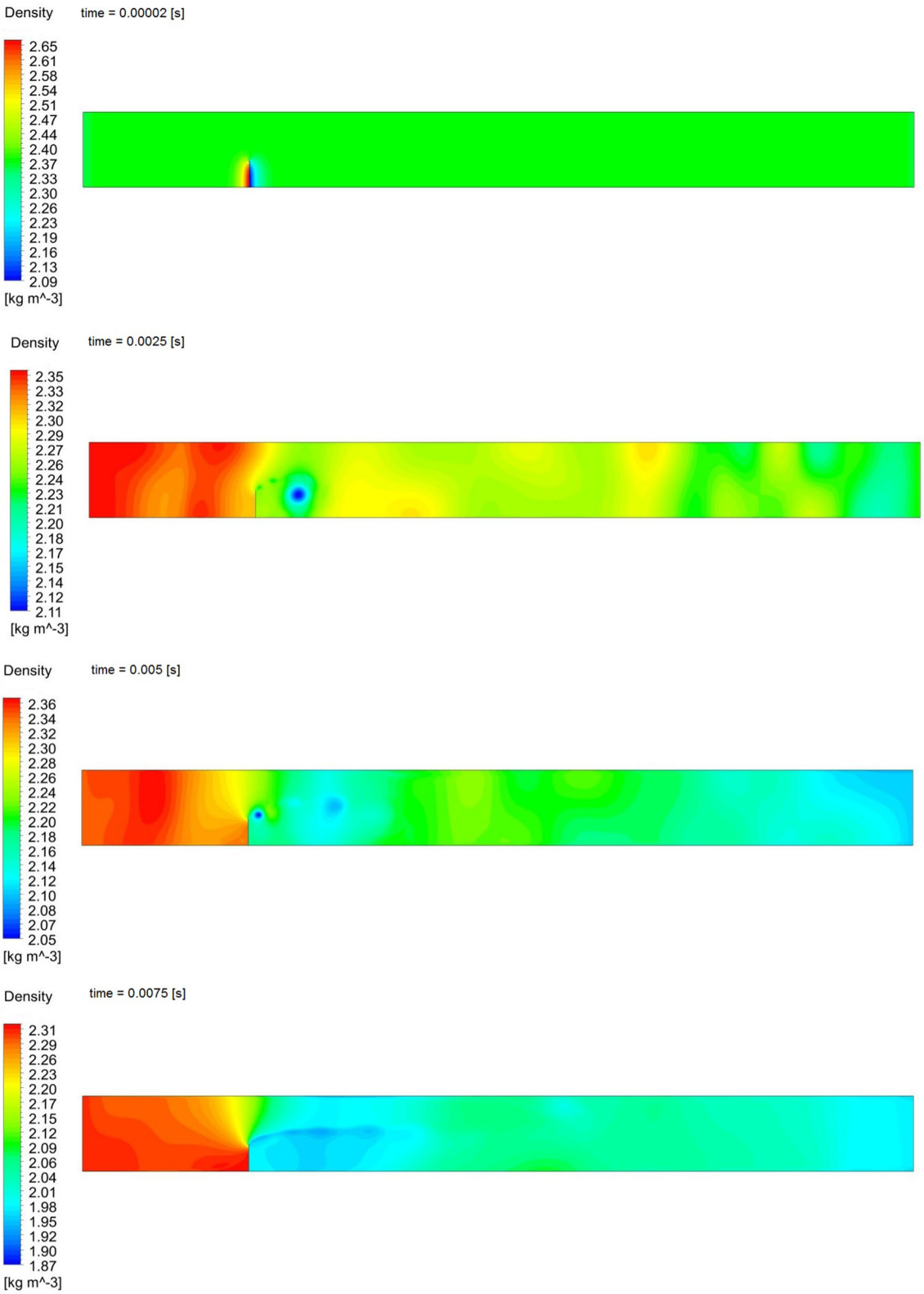

Fig. 20 Density distribution along the entire computational geometry at the time points = 0.00002, 0.0025, 0.005, 0.0075

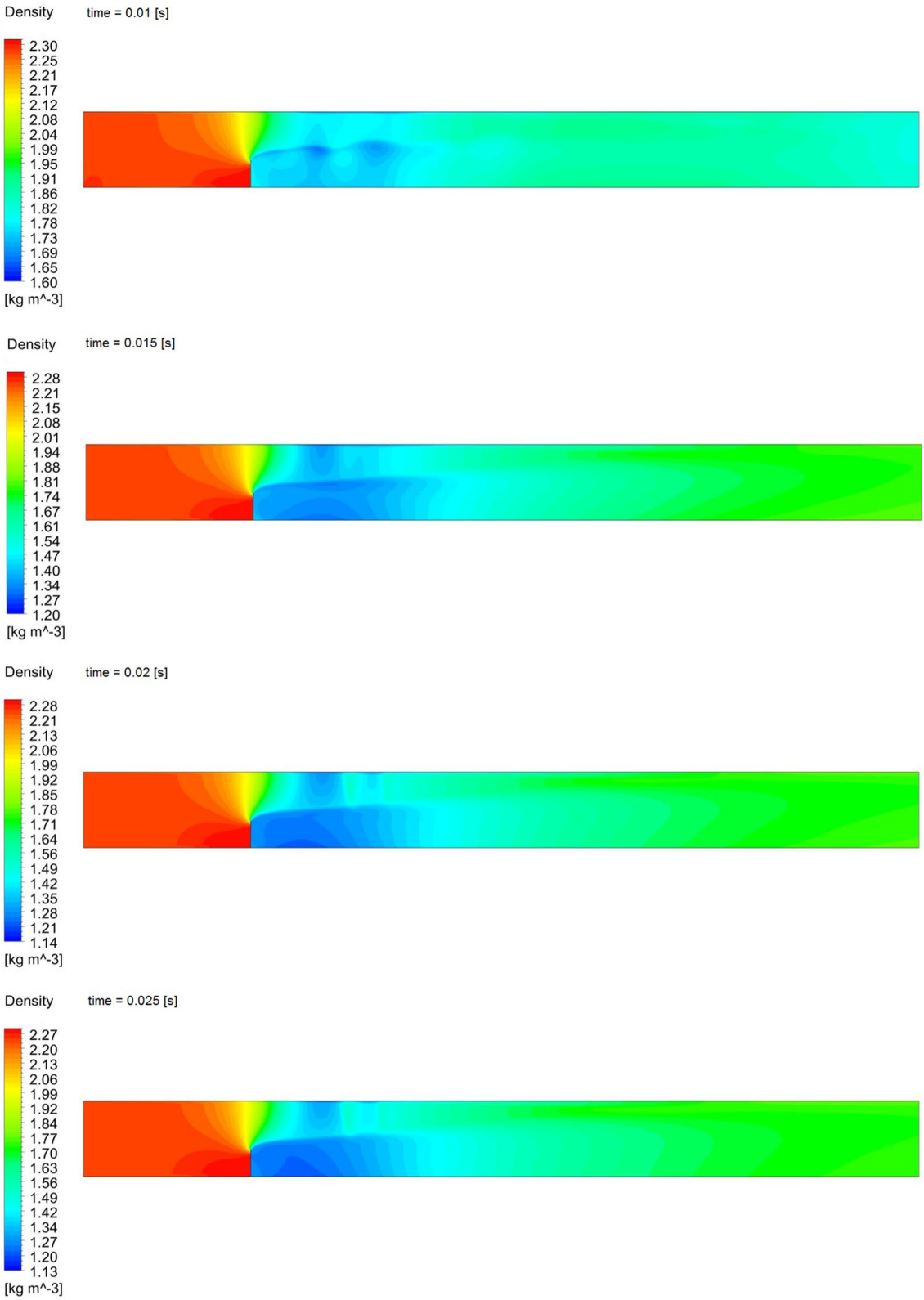

Fig. 21 Density distribution along the entire computational geometry at the time points = 0.01, 0.015, 0.02, 0.025

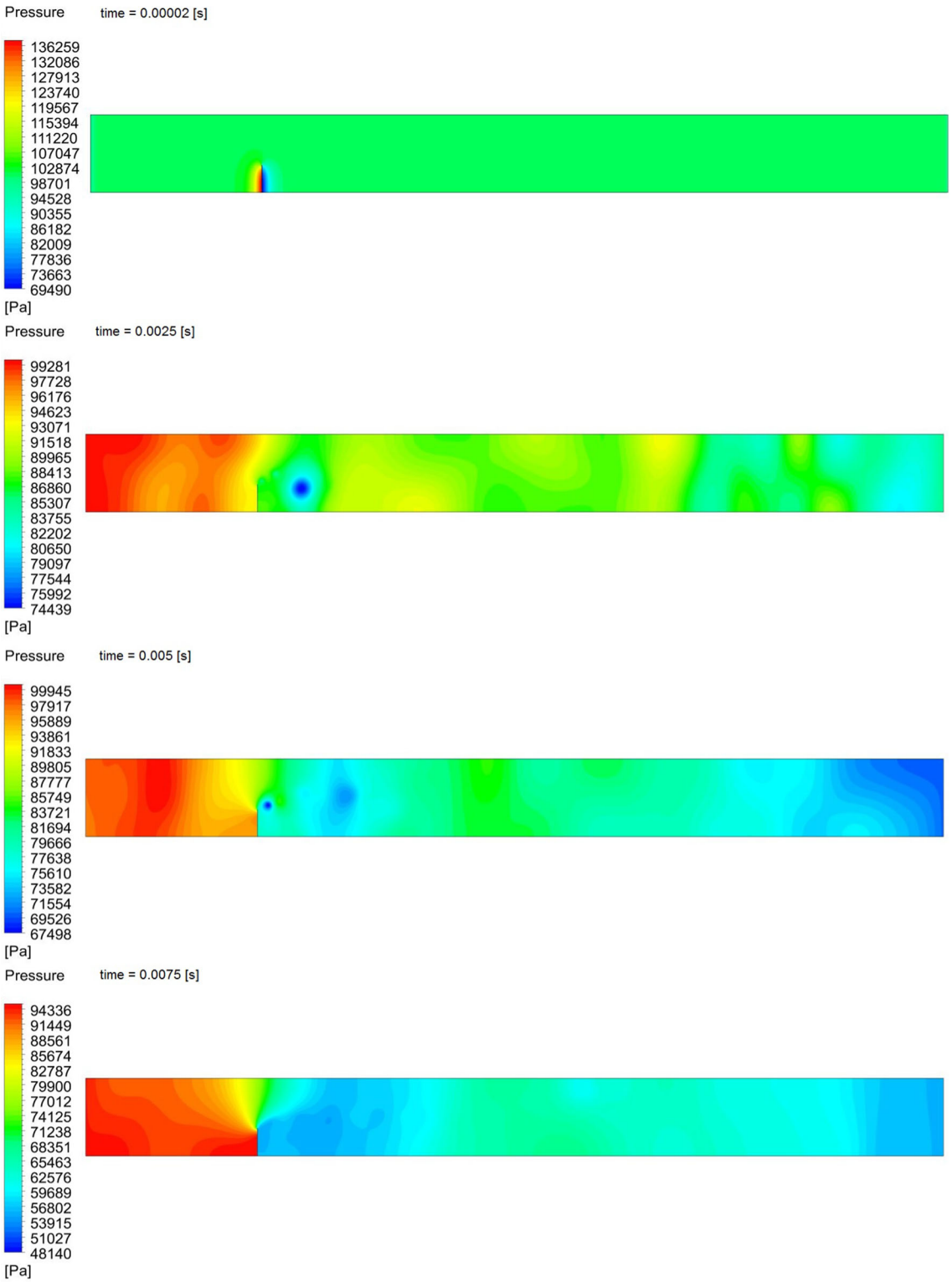

Fig. 22 Static pressure distribution along the entire computational geometry at the time points = 0.00002, 0.0025, 0.005, 0.0075

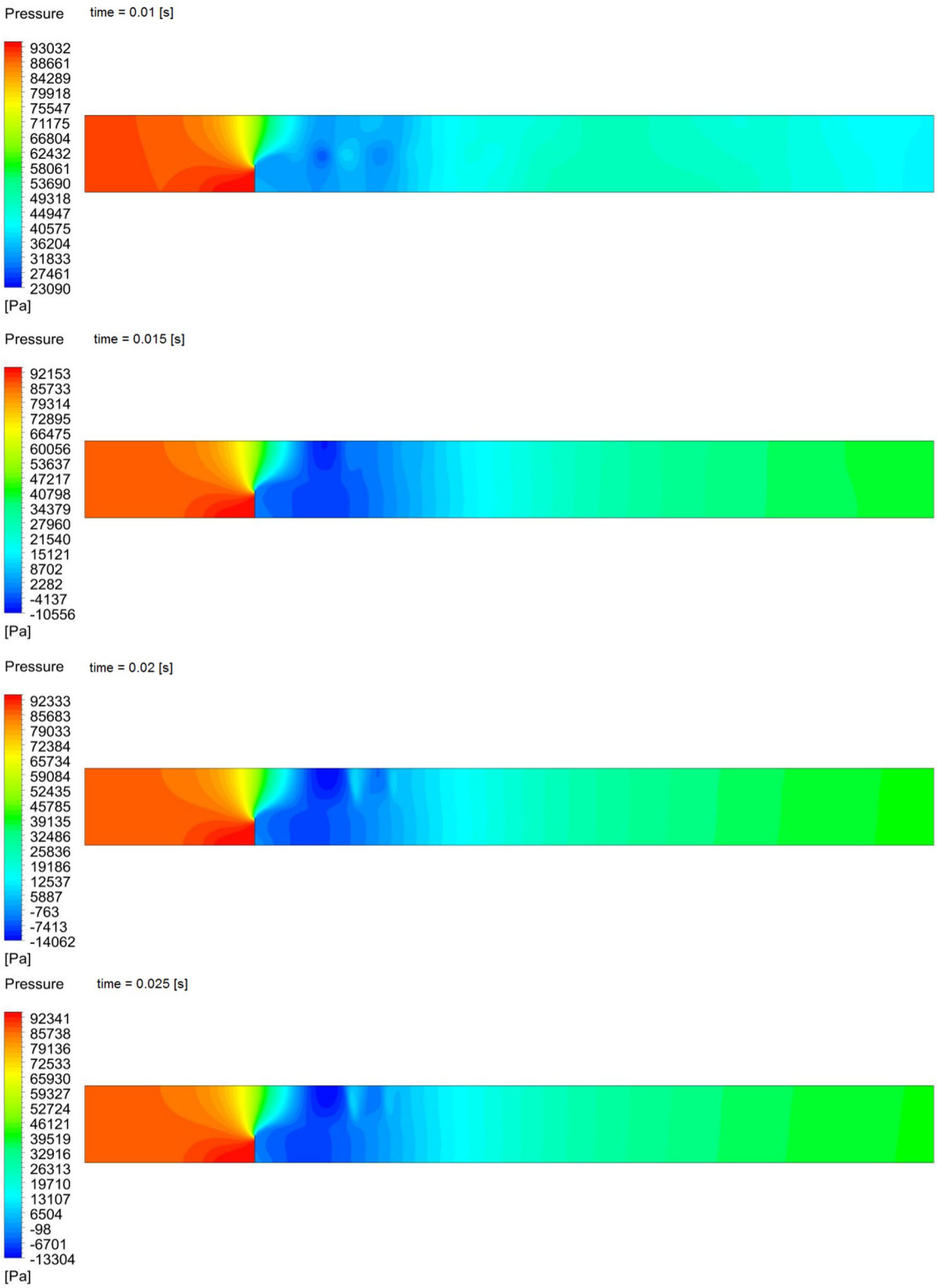

Fig. 23 Static pressure distribution along the entire computational geometry at the time points = 0.01, 0.015, 0.02, 0.025

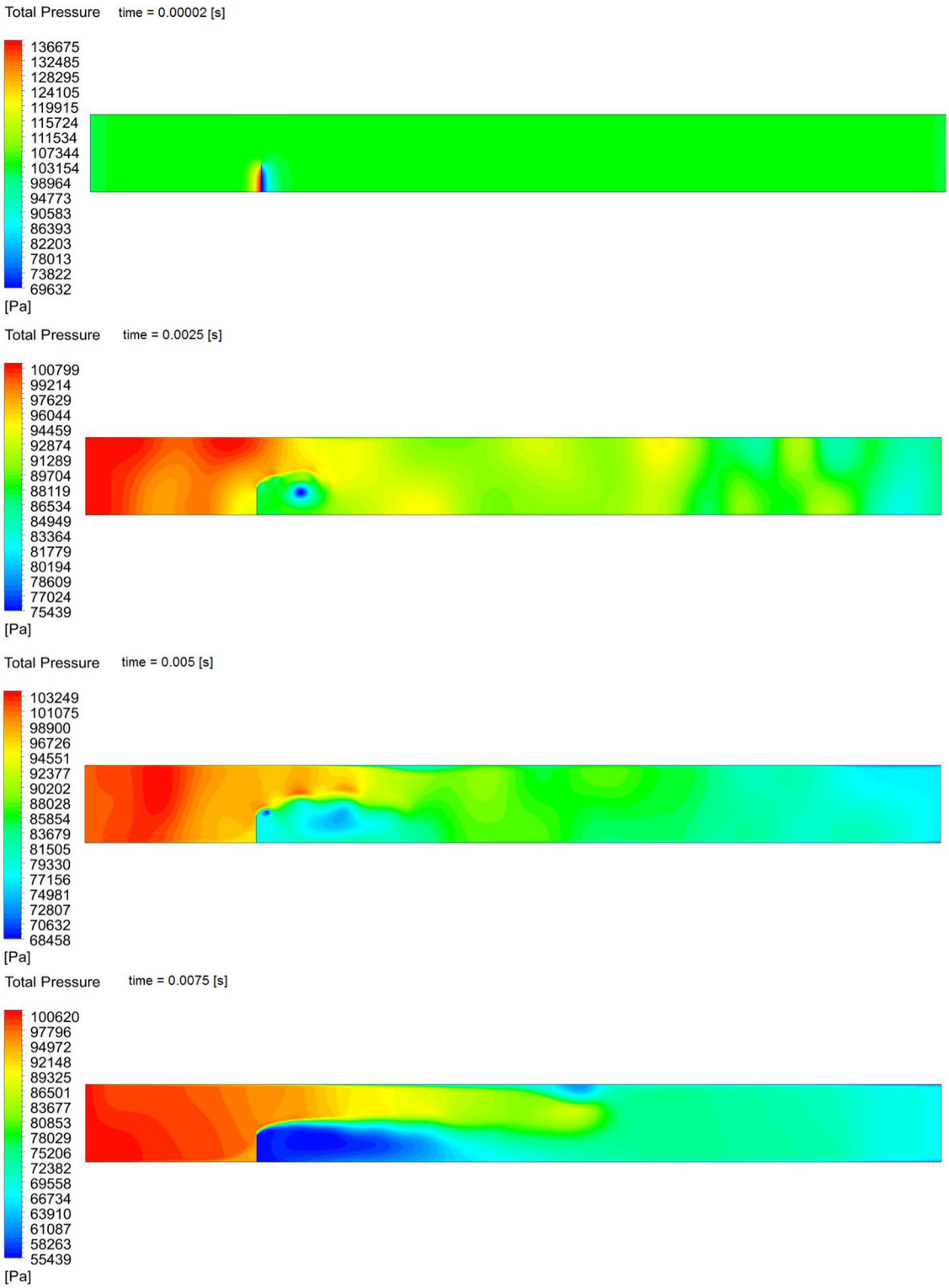

Fig. 24 Total pressure distribution along the entire computational geometry at the time points = 0.00002, 0.0025, 0.005, 0.0075

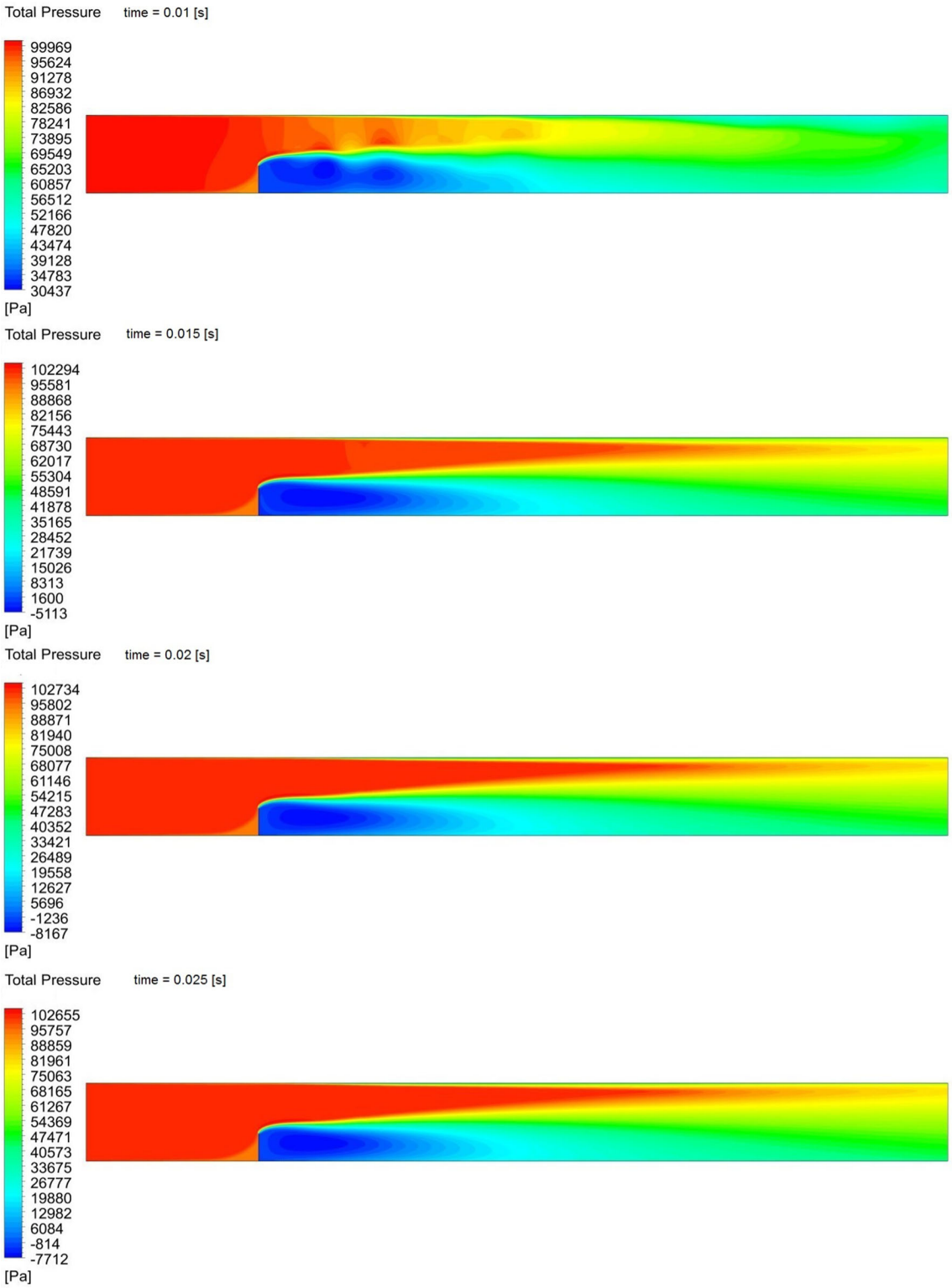

Fig. 25 Total pressure distribution along the entire computational geometry at the time points = 0.01, 0.015, 0.02, 0.025

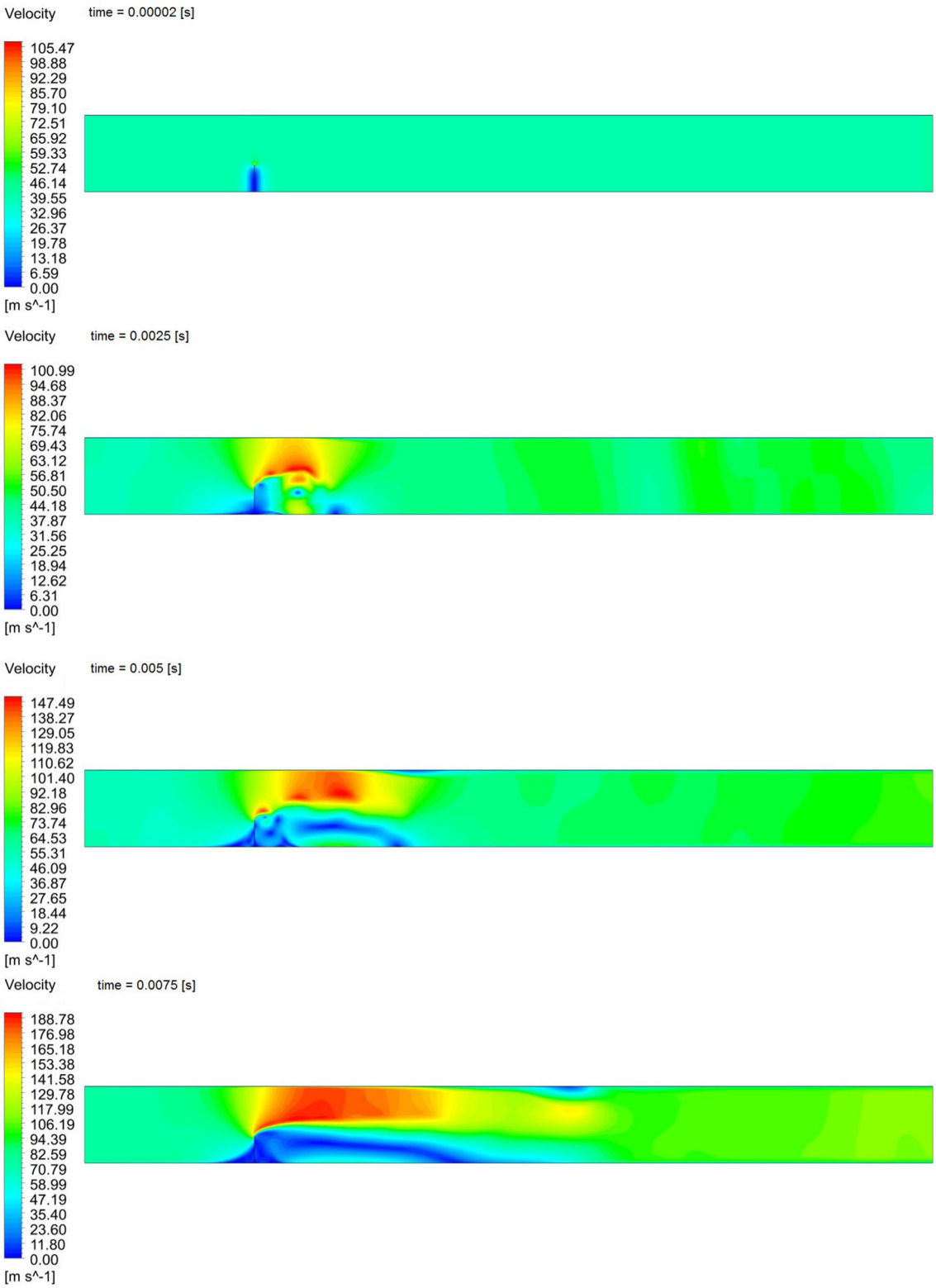

Fig. 26 Velocity distribution along the entire computational geometry at the time points = 0.00002, 0.0025, 0.005, 0.0075

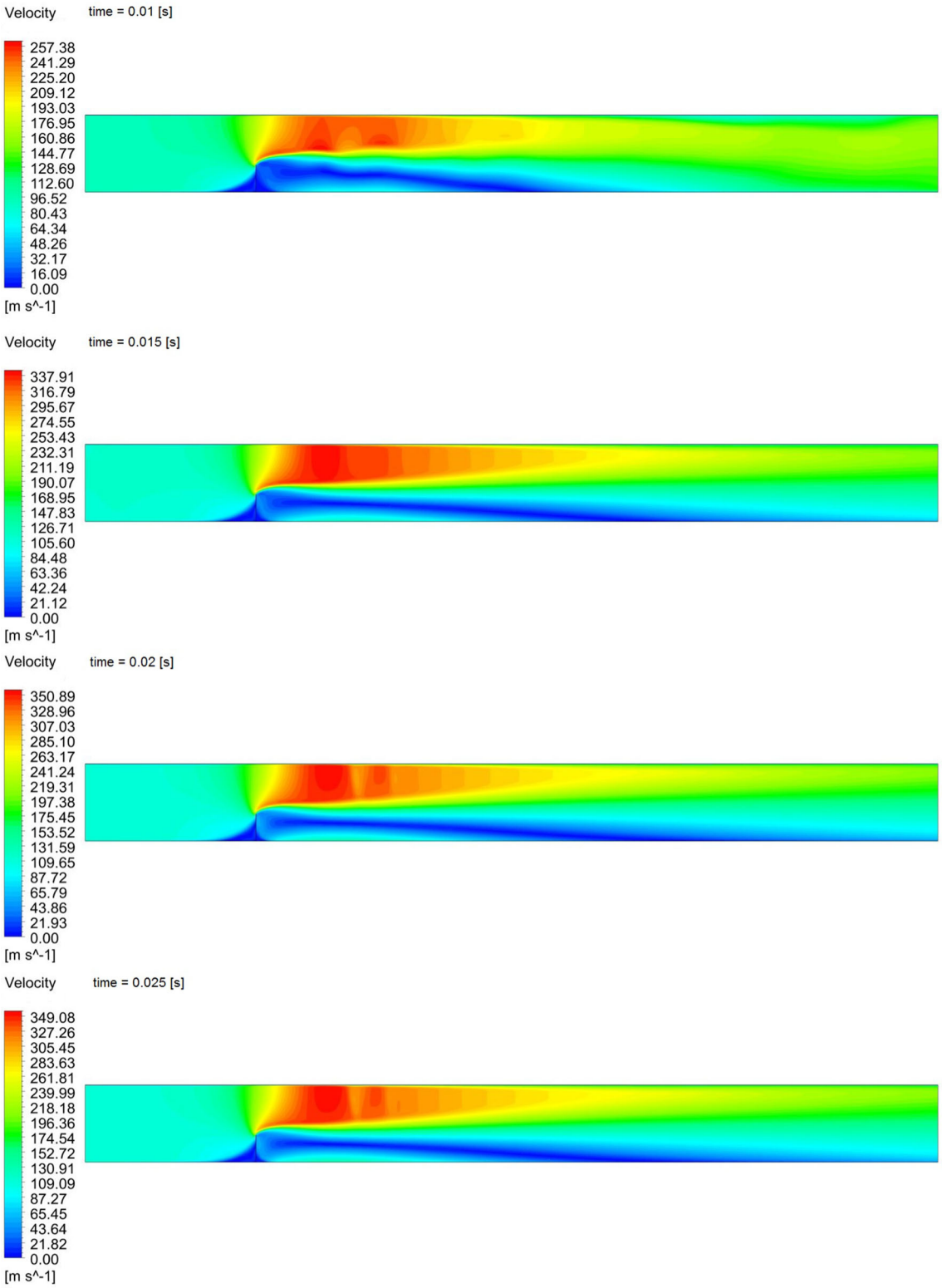

Fig. 27 Velocity distribution along the entire computational geometry at the time points = 0.01, 0.015, 0.02, 0.025

References

1. Wang, X.S.: Fundamentals of Fluid-Solid Interactions: Analytical and Computational Approaches, vol. 592. Elsevier, Amsterdam (2008)
2. Hodges, D.H., Pierce, G.A.: Introduction to Structural Dynamics and Aeroelasticity (Vol. 15), vol. 247. Cambridge University Press, Cambridge (2011)
3. Dowell, E.H. (ed.): A Modern Course in Aeroelasticity, vol. 720. Springer, New York (2004)
4. Bukowski, J.: Fluid Mechanics (in Polish), vol. 444. PWN, Warsaw (1959)
5. Flaga, A.: Basics of Solid and Fluid Mechanics (in Polish), vol. 596. PWN, Warszawa (2019)
6. Kim, J.H., Kim, H.D., Park, K.A.: Computational/experimental study of a variable nozzle flow. Flow Meas. Instrum. **17**, 81–86 (2006)
7. Kim, H.D., Lee, J.H., Park, K.A., Setoguchi, T., Matsuo, S.: A study of the critical nozzle for flow rate measurement of high-pressure hydrogen gas. J. Therm. Sci. **16**(1), 28–32 (2007)
8. Bathe, K.J., Hahn, W.F.: On transient analysis of fluid-structure systems. Comput. Struct. **10**, 383–391 (1978)
9. Luongo, A., Piccardo, G.: Linear instability mechanisms for coupled translational galloping. J. Sound Vib. **288**, 1027–1047 (2005)
10. Piccardo, G., Carassale, L., Freda, A.: Critical conditions of galloping for inclined square cylinders. J. Wind Eng. Ind. Aerodyn. **99**, 748–756 (2011)
11. Pagnini, L.C., Freda, A., Piccardo, G.: Uncertainties in the evaluation of one degree-of-freedom galloping onset. Eur. J. Environ. Civ. Eng. **21**(7–8), 1043–1063 (2017)
12. Pagnini, L.C., Piccardo, G.: A generalized gust factor technique for evaluating the wind-induced response of aeroelastic structures sensitive to vortex-induced vibrations. J. Fluids Struct. **70**, 181–200 (2017)
13. Piccardo, G., Tubino, F., Luongo, A.: On the effect of mechanical non-linearities on vortex-induced lock-in vibrations. Math. Mech. Solids **22**(10), 1922–1935 (2017)
14. Piccardo, G., Zulli, D., Luongo, A.: Dry galloping in inclined cables: linear stability analysis. Procedia Eng. **199**, 3164–3169 (2017)
15. Giorgio, I.: A variational formulation for one-dimensional linear thermo-viscoelasticity. Math. Mech. Complex Syst. **9**(4), 397–412 (2021)
16. Giorgio, I.: A discrete formulation of Kirchhoff rods in large-motion dynamics. Math. Mech. Solids **25**(5), 1081–1100 (2020)
17. Blom, F.J., Leyland, P.: Analysis of fluid–structure interaction by means of dynamic unstructured meshes. Trans. ASME **120**, 792–798 (1998)
18. Białobrzeski, I., Zielińska, M., Mujumdar, A.S., Markowski, M.: Heat and mass transfer during drying of a bed of shrinking particles—simulation for carrot cubes dried in a spout-fluidized-bed drier. Int. J. Heat Mass Transf. **51**, 4704–4716 (2008)
19. Fernandez, M.A., Moubachir, M.: A Newton method sing exact Jacobians for solving fluid-structure coupling. Comput. Struct. **83**, 127–142 (2005)
20. Taciroglu, E., Acharya, A., Namazifard, A., Parsons, I.D.: Arbitrary Lagrangian–Eulerian methods for analysis of regressing solid domains and interface tracking. Comput. Struct. **87**, 355–367 (2009)
21. Kuhl, E., Steinmann, P.: A hyperelastodynamic ALE formulation based on referential, spatial and material settings of continuum mechanics. Acta Mech. **174**, 201–222 (2005)
22. Banaś, K.: Modelling of heat exchange in fluid flow machinery using coupled heat exchange tools and fluid-solid interaction tools (in polish). Ph.D thesis, IMP PAN. Gdańsk 2017
23. Piperno, S., Farhat, C., Larrouturou, B.: Partitioned procedures for the transient solution of coupled aeroelastic problems. Part I: model problem, theory and two dimensional application. Comput. Methods Appl. Mech. Eng. **124**, 79–112 (1995)
24. Farhat, C., Lesoinne, M., Maman, N.: Mixed explicit/implicit time integration of coupled aeroelastic problems: there-field formulation, geometric conservation and distributed solution. Int. J. Numer. Meth. Fluids **21**, 807–835 (1995)
25. Fahrat, C., Lesoinne, M.: Two efficient staggered algorithms for the serial and parallel solution of three-dimensional nonlinear transient aeroelastic problems. Comput. Methods Appl. Mech. Eng. **182**, 499–515 (2000)
26. Fahrat, C., Van der Zee, K.G., Geuzaine, P.: Provably second-order time accurate loosely-coupled solution algorithms for transient nonlinear computational aeroelasticity. Comput. Methods Appl. Mech. Eng. **195**, 1973–2001 (2006)
27. Vaze, M., Haiyan, M., Gopalan, H., Joo, P.H., Jing, L.: Methodology Development for Wind Driven Cantiliver Vibration using Fluent-Structural Interaction. World Congress on Computational Mechanics XII, Seoul, Korea (2016)
28. Matthies, H.G., Steindorf, J.: Partitioned strong coupling algorithms for fluid–structure interaction. Comput. Struct. **81**, 805–812 (2003)
29. Dettmer, W.G., Perić, D.: On the coupling between fluid flow and mesh motion in the modelling of fluid–structure interaction. Comput. Mech. **43**, 81–90 (2008)
30. Hou, G., Wang, J., Layton, A.: Numerical methods for fluid–structure interaction—a review. Commun. Comput. Phys. **12**, 337–377 (2012)
31. Donea, J., Fasoli-Stella, P., Cook J.L.: Lagrangian and Eulerian finite element techniques for transient fluid–structure interaction problems. Paper B1/2. Trans. 4thSMiRT Conf., San Francisco, 1977
32. Belytschko, T., Kennedy, J.M.: Computer models for subassembly simulation. Nucl. Eng. Des. **49**, 17–38 (1978)
33. Hughes, T.H.J., Liu, W.L., Zimmermann, T.K.: Lagrangian–Eulerian finite element formulation for incompressible viscous flows. Comput. Methods Appl. Mech. Eng. **29**(3), 329–349 (1981)
34. Truesdell, C., Noll, W.: The Non-linear Field Theories of Mechanics, vol. 629. Springer, Berlin (2004)
35. Chróścielewski, J., Schmidt, R., Eremeyev, V.A.: Nonlinear finite element modeling of vibration control of plane rod-type structural members with integrated piezoelectric patches. Continuum Mech. Thermodyn. **31**, 147–188 (2019)
36. Bruski, D., Burzyński, S., Chróścielewski, J., Pachocki, Ł, Wilde, K., Witkowski, W.: The influence of position of the post or its absence on the performance of the cable barrier system. MATEC Web of Conference **219**, 02012 (2018)
37. Luongo, A., Rega, G., Vestroni, F.: Planar non-linear free vibrations of an elastic cable. Int. J. Non-Linear Mech. **19**(1), 39–52 (1984)

38. Ferretti, M., Zulli, D., Luongo, A.: A continuum approach to the nonlinear in-plane galloping of shallow flexible cables. Adv. Math. Phys. **2**, 1–12 (2019)
39. Luongo, A., Zull, D.: Statics of shallow inclined elastic cables under general vertical loads: a perturbation approach. Mathematics **6**(2), 24 (2018)
40. Ferretti, M., Piccardo, G., dell'Isola, F., Luongo, A.: Dynamics of taut strings undergoing large changes of tension caused by a force-driven traveling mass. J. Sound Vib. **458**, 320–333 (2019)
41. Ferretti, M., Piccardo, G., Luongo, A.: Semi-analytical approaches for the nonlinear dynamics of a taut string subject to a moving load. Nonlinear Dyn. **98**(4), 2463–2474 (2019)
42. Ferretti, M., Gavrilov, S.N., Eremeyev, V.A., Luongo, A.: Nonlinear planar modeling of massive taut strings travelled by a force-driven point-mass. Nonlinear Dyn. **97**(4), 2201–2218 (2019)
43. Hirsch, C.: Numerical Computation of Internal and External Flows Volume 1 Fundamentals of Computational Fluid Dynamics, vol. 696. John Wiley & Sons Ltd, Oxford (2007)
44. Badur, J.: Numerical Modeling of Sustainable Combustion in Gas Turbines, vol. 259. IFFM Publishers, Gdańsk (2003)
45. Badur, J.: Five Lectures of Contemporary Fluid Thermomechanics, vol. 267, 2nd edn. IFFM PAS, Gdańsk (2005). (**in Polish**)
46. Dudda, W.: Numerical modelling of a structure corrosive degradation during workcycles. Lett. Inst. Fluid-Flow Mach. Polish Acad. Sci. **1456**, 1–144 (2005). Gdansk (in Polish)
47. Badur, J., Ziółkowski, P., Kornet, S., Kowalczyk, T., Banaś, K., Bryk, M., Ziółkowski, P.J., Stajnke, M.: Enhanced energy conversion as a result of fluid-solid interaction in micro- and nanoscale. JTAM **56**(1), 329–332 (2018)
48. Ziółkowski, P., Badur, J.: On Navier slip and Reynolds transpiration numbers. Arch. Mech. **70**(3), 269–300 (2018)
49. Spalart, P.R., Allmaras, S.R.: A one equation model for aerodynamics flows. La Rech. Aerosp. **1**, 5–21 (1994)
50. Badur, J., Karcz, M., Lemański, M.: On the mass and momentum transport in the Navier–Stokes slip layer. Microfluid. Nanofluid. **10**, 32–61 (2011)
51. Badur, J., Ziółkowski, P., Zakrzewski, W., Sławiński, D., Banaszkiewicz, M., Kaczmarczyk, O., Kornet, S & Ziółkowski, P.J.: On the surface vis impressa caused by fluid-solid contact. Shell Structures: Theory and Applications, vol. 3, pp. 53–56. Pietraszkiewicz & Góski (Eds) Taylor & Francis Group, London (2014)
52. Javili, A., dell'Isola, F., Steinmann, P.: Geometrically nonlinear higher-gradient elasticity with energetic boundaries. J. Mech. Phys. Solids **61**, 2381–2401 (2013)
53. Ziółkowski, P.J., Ochrymiuk, T., Eremeyev, V.A.: Adaptation of the arbitrary Lagrange–Euler approach to fluid-solid interaction on an example of high velocity flow over thin platelet. Continuum Mech. Termodyn. (2019). https://doi.org/10.1007/s00161-019-00850-7
54. Zienkiewicz, O.C.: Finite Element Method, vol. I, II, III. Elsevier, Amsterdam (2005)
55. Newmark, N.M.: A method of computation for structural dynamics. J. Eng. Mech. Div. ASCE **85**(EM3), 67–94 (1959)
56. Sutherland, W.: The viscosity of gases and molecular force, Philosophical Magazine Series 5, 36:223, 507-531 (1893)